

Spectroscopy and Renormalisation Group Flow of a Lattice Nambu–Jona-Lasinio Model

A. Ali Khan^a, M. Göckeler^{a,b}, R. Horsley^{a,c},
P.E.L. Rakow^d, G. Schierholz^{a,c} and H. Stüben^{d,e}

^a Gruppe Theorie der Elementarteilchen,
Höchstleistungsrechenzentrum HLRZ,
c/o Forschungszentrum Jülich,
Postfach 1913, D-52425 Jülich, Germany

^b Institut für Theoretische Physik, RWTH Aachen,
Sommerfeldstraße, D-52056 Aachen, Germany

^c Deutsches Elektronen-Synchrotron DESY,
Notkestraße 85, D-22603 Hamburg, Germany

^d Institut für Theoretische Physik, Freie Universität Berlin,
Arnimallee 14, D-14195 Berlin, Germany

^e Address after 1 January 1994:
Konrad-Zuse-Zentrum für Informationstechnik Berlin,
Heilbronner Straße 10, D-10711 Berlin, Germany

Abstract

We investigate a lattice Nambu–Jona-Lasinio model both by the Monte Carlo method and Schwinger-Dyson equations. A comparison allows the discussion of finite size effects and the extrapolation to infinite volume. We pay special attention to the identification of particles and resonances. This enables us to discuss renormalisation group flows in the neighbourhood of the critical coupling where the chiral symmetry breaking phase transition takes place. In no region of the bare parameter space do we find renormalisability for the model.

1 Introduction

The study of four fermion interactions has a long history. Fermi originally introduced the idea as a theory for weak interactions [1]. Later Nambu and Jona-Lasinio proposed their model [2] (in the following called the NJL model) to describe spontaneous chiral symmetry breaking and dynamical mass generation. This was one of the first works to note the association of a massless Nambu-Goldstone boson with the spontaneous breaking of a continuous symmetry [3].

Over the years there have been efforts to investigate the vacuum structure of strongly interacting four fermion theories [4]. Recently there has been renewed interest in this subject in connection with technicolour and the top-mode standard model [5, 6]. For these applications one is mainly interested in the physics of the broken phase where the fermion mass is dynamically generated. Additional interest was generated by the discovery that a generalized NJL model is equivalent to the Higgs-Yukawa model [7, 8] and possibly to $SU(N)$ gauge theory [9]. Furthermore there have been various investigations of the gauged NJL model [10] which show a line of second order phase transitions linking the pure NJL model and QED. This raises the question of whether the two models fall into the same universality class. Our investigation of QED [11] has shown that in the strong coupling regime (including the critical region) it is impossible to vary the cutoff without changing the physics, while in the weakly coupled region this is possible. We have called such behaviour weak renormalisability.

In this paper we are mainly interested in the model's phase transition and critical behaviour. Since this falls into the large coupling region, nonperturbative methods are required. We use the lattice Monte Carlo simulation and the semi-analytic Schwinger-Dyson method [12, 13]. The Monte Carlo method has the advantage of being exact but can only be applied on finite lattice volumes. The Schwinger-Dyson approach on the other hand can be extended to infinite volumes but suffers from having an uncontrolled approximation. The synergy of both methods allows us to go much further than with either method alone.

We have looked at the chiral condensate in order to map out the phase diagram. We find a second order chiral phase transition implying infinite correlation length which in principle allows us to obtain a continuum theory. In the vicinity of the critical point we calculate the renormalised fermion mass (μ_R) and the energy levels of the pseudoscalar (π , Goldstone boson), scalar (σ) and vector (ρ) fermion-antifermion composite states as well as the pion decay constant (f_π).

A major problem is the identification of resonances and bound states on a finite lattice. For the π and ρ we were able to identify the first excited energy levels by our Monte Carlo calculation. These compare favourably with the results from the Schwinger-Dyson equations. Thus we feel encouraged to take the thermodynamic limit of the Schwinger-Dyson equations. This allows the calculation of the spectral functions and thus the identification of resonances. With this identification at hand we construct flow diagrams of dimensionless

ratios of physical quantities. We use them to investigate the renormalisation group flow in the vicinity of the critical point.

The paper is organized as follows. Our lattice model is defined in section 2.1. Details of the Monte Carlo method are given in sections 2.2, 3.1, 3.2 and 4.1 (see also [14]). The Schwinger-Dyson equations are discussed in sections 2.3, 3.2, 3.3, 4.2, 4.3 and the appendices. Our main results of both methods are given in section 5 on meson spectroscopy and in section 6 for the renormalisation group flows. Finally in section 7 we present our conclusions.

2 The Model

Because we are interested in chiral symmetry properties we use staggered fermions throughout.

2.1 The Action

The NJL model is defined by the continuum action

$$S = \int d^4x \left\{ \bar{\psi}(x) \gamma_\mu \partial_\mu \psi(x) - g_0 \left[\left(\bar{\psi}(x) \psi(x) \right)^2 - \left(\bar{\psi}(x) \gamma_5 \psi(x) \right)^2 \right] \right\} \quad (2.1)$$

which is chirally invariant. For staggered fermions we take the action

$$\begin{aligned} S &= \frac{1}{2} \sum_{x,\mu} \eta_\mu(x) [\bar{\chi}(x) \chi(x + \hat{\mu}) - \bar{\chi}(x + \hat{\mu}) \chi(x)] + m_0 \sum_x \bar{\chi}(x) \chi(x) \\ &- g_0 \sum_{x,\mu} \bar{\chi}(x) \chi(x) \bar{\chi}(x + \hat{\mu}) \chi(x + \hat{\mu}), \end{aligned} \quad (2.2)$$

where

$$\eta_\mu(x) = (-1)^{x_1 + \dots + x_{\mu-1}}, \quad \eta_1(x) = 1. \quad (2.3)$$

The interaction is chosen as the simplest one that is invariant under the continuous chiral transformation

$$\chi(x) \rightarrow e^{i\alpha\epsilon(x)} \chi(x), \quad \bar{\chi}(x) \rightarrow e^{i\alpha\epsilon(x)} \bar{\chi}(x), \quad (2.4)$$

with

$$\epsilon(x) = (-1)^{x_1 + x_2 + x_3 + x_4}. \quad (2.5)$$

The mass term acts as a chiral symmetry breaking external source and as an infrared regulator.

2.2 Monte Carlo Simulation

In order to use the Monte Carlo method we first have to integrate out the fermion fields. Therefore we have to rewrite the interaction in a bilinear form. This is done by introducing an auxiliary field $\theta_\mu(x) \in [0, 2\pi)$ [15, 16]:

$$S_{\text{int}} = \sqrt{g_0} \sum_{x,\mu} \eta_\mu(x) \left[\bar{\chi}(x) e^{i\theta_\mu(x)} \chi(x + \hat{\mu}) - \bar{\chi}(x + \hat{\mu}) e^{-i\theta_\mu(x)} \chi(x) \right]. \quad (2.6)$$

The Hybrid Monte Carlo method was employed to generate the configurations. Lattices of size $V = L_s^3 \times L_t = 6^3 \times 12, 8^4, 8^3 \times 16, 8^3 \times 32$ and 12^4 were used. Boundary conditions were periodic in the spatial directions and anti-periodic in the time direction. We investigated the model for $m_0 = 0.01$ to 0.09 and $g_0 = 0.21$ to 0.32 . For each parameter set 1000 trajectories were generated for measurements. The trajectory length was always ≈ 0.8 . The number of time steps was adjusted such that acceptance rates between 70 and 80% were achieved. Propagators were calculated with the conjugate gradient method. As convergence criterion we required that the norm of the rest vector was smaller than 10^{-5} . The chiral condensate was calculated with a stochastic estimator (see, e. g., [17]).

2.3 Schwinger-Dyson Equations

The model (2.2) was also studied by solving truncated Schwinger-Dyson equations up to order g_0 and g_0^2 on the lattice. To make a direct comparison with Monte Carlo results possible we use the same action with the same cut-off (for another application of Schwinger-Dyson equations to a lattice theory see [18]).

In order to write the equations in this section in a compact form it is useful to give the lattice action (2.2) with a slightly different notation:

$$S = \sum_{\mu} \bar{\chi}_x d_{\mu}^{x,y} \chi_y + m_0 \bar{\chi}_x \chi_x - g_0 \bar{\chi}_x \chi_{x'} c_{x'y'}^{x,y} \bar{\chi}_y \chi_{y'}. \quad (2.7)$$

The fields at site x are $\bar{\chi}_x$ and χ_x , and the Einstein summation convention is to be used whenever a site index occurs twice. The meaning of the kinetic matrices d^{μ} and of the coupling tensor $c_{x'y'}^{x,y}$ should be clear by comparison with (2.2): $d^{\mu} \frac{x}{y} = +\frac{1}{2}\eta_{\mu}(x)$ if $y = x + \hat{\mu}$, $d^{\mu} \frac{x}{y} = -\frac{1}{2}\eta_{\mu}(x)$ if $y = x - \hat{\mu}$ and zero otherwise; $c_{x'y'}^{x,y} = 1$ if $x = x'$, $y = y'$ and x and y are neighbours, and is zero otherwise. It is convenient to give the coupling tensor four indices so that we can use the Einstein summation convention and to remind us that more general four-fermi coupling terms are possible.

The lattice Feynman rules are that the bare staggered fermion propagator is

$$G^{\text{bare}} = \left(m_0 \delta_y^x + \sum_{\mu} d^{\mu} \frac{x}{y} \right)^{-1}, \quad (2.8)$$

and the vertex is

$$-g_0 c_{x'y'}^{x,y}. \quad (2.9)$$

When the interaction is turned on the bare fermion propagator is replaced by the full fermion propagator

$$G^{\text{full}} = \left(M_y^x + \sum_{\mu} D^{\mu} \frac{x}{y} \right)^{-1}. \quad (2.10)$$

The new matrices M_y^x and $D^{\mu} \frac{x}{y}$ are generalisations of the matrices $m_0 \delta_y^x$ and $d^{\mu} \frac{x}{y}$ appearing in (2.8) and have the same symmetries, e. g., M_y^x is symmetric under reflections and links sites with even separations in violation of chiral symmetry. On the other hand $D^{\mu} \frac{x}{y}$ is odd in the μ direction and even in the other directions and only links sites with odd separations and so respects chiral symmetry. M is invariant under translations, D^{μ} acquires the same factors of ± 1 as d^{μ} .

In fig. 1 we show graphically the Schwinger-Dyson equations for the fermion propagator. It is not possible to solve the full Schwinger-Dyson equations. They have to be truncated at some stage. The crudest approximation is to keep only term (a) which gives the gap equation, namely

$$\begin{aligned} D^{\mu} \frac{x}{y} &= d^{\mu} \frac{x}{y}, \\ M_y^x &= N \delta_y^x, \end{aligned} \quad (2.11)$$

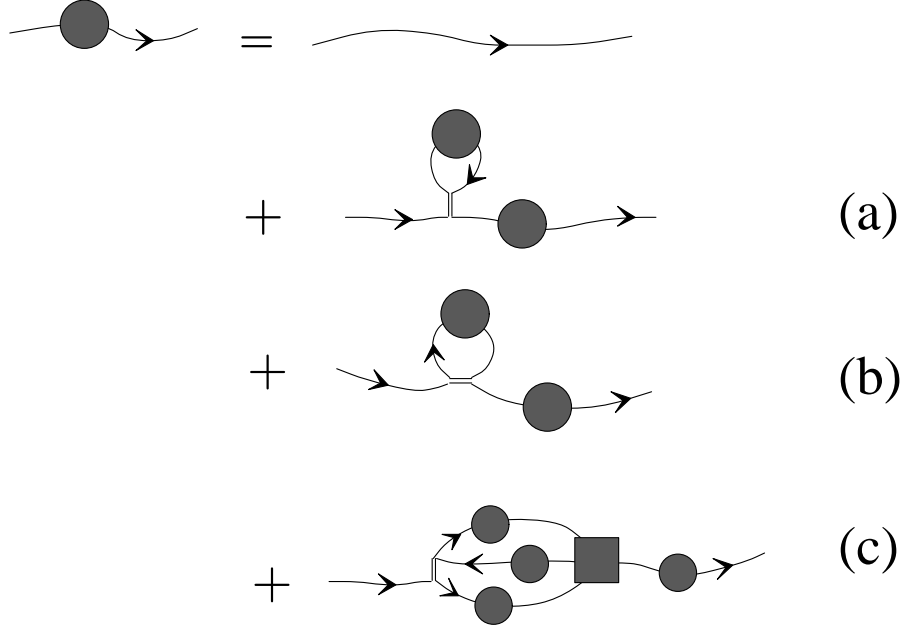


Figure 1: *Pictorial representation of the Schwinger-Dyson equation for the fermion propagator.*

where N satisfies

$$N = m_0 + 8g_0 \frac{1}{V} \sum_k \frac{N}{N^2 + \sum_\nu \sin^2 k_\nu}. \quad (2.12)$$

The k -sum runs over all momenta consistent with the boundary conditions. The fermion mass μ_R is given by the position of the pole and is $\mu_R = \sinh^{-1} N$.

The next approximation is to keep terms (a) and (b). Term (a) leads simply to a renormalisation of the mass and term (b) leads to a renormalisation of the kinetic energy. We shall call these the order g_0 Schwinger-Dyson equations because the error is of order g_0^2 . Explicitly they read

$$\begin{aligned} D_y^\mu{}^x &= F_\mu d_y^\mu{}^x, \\ M_y^x &= N \delta_y^x, \end{aligned} \quad (2.13)$$

where N and F satisfy

$$\begin{aligned} N &= m_0 + 8g_0 \frac{1}{V} \sum_k \frac{N}{N^2 + \sum_\nu F_\nu^2 \sin^2 k_\nu}, \\ F_\mu &= 1 + 2g_0 \frac{1}{V} \sum_k \frac{F_\mu \sin^2 k_\mu}{N^2 + \sum_\nu F_\nu^2 \sin^2 k_\nu}. \end{aligned} \quad (2.14)$$

The pole position giving the fermion mass is

$$\mu_R = \sinh^{-1} \frac{N}{F_t}. \quad (2.15)$$

In infinite volumes (when the sum is replaced by an integral) F needs no direction index, as all the F_μ 's are identical. However in a finite system with different lattice lengths and boundary conditions in the space and time directions an index is needed.

The order g_0^2 equations also include term (c), but with the full vertex replaced by the bare vertex, an approximation which introduces an error of $O(g_0^3)$. The resulting equations (given in configuration space) are

$$\begin{aligned}
M_y^x + \sum_{\mu} D_{\mu}^{\mu x} &= m_0 \delta_y^x + \sum_{\mu} d_{\mu}^{\mu x} \\
&+ g_0 c_{yv}^{xu} G_u^{\text{full} v} - g_0 c_{vy}^{xu} G_u^{\text{full} v} \\
&- g_0^2 c_{vr}^{xu} G_s^{\text{full} r} G_u^{\text{full} z} G_w^{\text{full} v} c_{zy}^{sw} \\
&+ g_0^2 c_{vr}^{xu} G_w^{\text{full} r} G_u^{\text{full} z} G_s^{\text{full} v} c_{zy}^{sw}. \tag{2.16}
\end{aligned}$$

M and D can be projected out by using their different behaviours under reflection. For the first time the unknown matrices M and D are not simply renormalised versions of the bare matrices, but extend further in space. Mass and wave-function normalisation become momentum dependent. The matrices M_y^x and D_y^x are stored in position space. These individual components can be thought of as the Fourier coefficients for the momentum space fermion propagator.

The equations were solved numerically by simple iterations. Typically about 7 iterations were needed in the order g_0 case to obtain convergence and 20–40 iterations in the order g_0^2 case.

3 Chiral Condensate and Fermion Mass

3.1 Phase Diagram

To find the phase diagram we have computed the chiral condensate $\langle \bar{\chi}\chi \rangle$ also referred to as σ . Monte Carlo results are collected in tables 1 and 2. To show that we are working in the vicinity of the critical point we look at a Fisher plot [19] of our data, i. e., we have plotted $\langle \bar{\chi}\chi \rangle^2$ against $m_0/\langle \bar{\chi}\chi \rangle$ in fig. 2. The lines connect points of constant g_0 . If the theory was mean-field like, these would be straight parallel lines [19]. We see that this is approximately the case for our data. For large g_0 the extrapolated lines end on the y -axis giving a finite value for $\langle \bar{\chi}\chi \rangle$ at $m_0 = 0$, while for small g_0 the extrapolated lines end on the x -axis giving zero for $\langle \bar{\chi}\chi \rangle$ at $m_0 = 0$. The line that corresponds to the critical coupling would end at the origin as is indicated by the dashed lines in fig. 2. On the $8^3 \times 16$ lattice this gives an estimate of about $0.25 < g_c < 0.26$ while on the 12^4 lattice g_c is somewhat larger than 0.27. We see from this that there are finite size effects in the data as can also be inferred from a cursory look at tables 1 and 2. We shall in the following call the region $g_0 < g_c$ the symmetric phase and the region $g_0 > g_c$ the broken phase.

In fig. 3 we compare our Monte Carlo data with results from the gap equation and our two Schwinger-Dyson approximations. (The chiral condensate is the value of the fermion propagator at zero distance: $\sigma = V^{-1} \sum_x G^{\text{full}}_{xx}$.) There is a large discrepancy between the numerical data and the gap equation. However the agreement improves considerably as higher orders are included leading to a maximum discrepancy of about 10% with our Monte Carlo data. The equations also reproduce the large finite size effects.

Applying the Schwinger-Dyson equations for infinite volume and zero bare mass reveals that there is a chiral phase transition and not just a crossover.

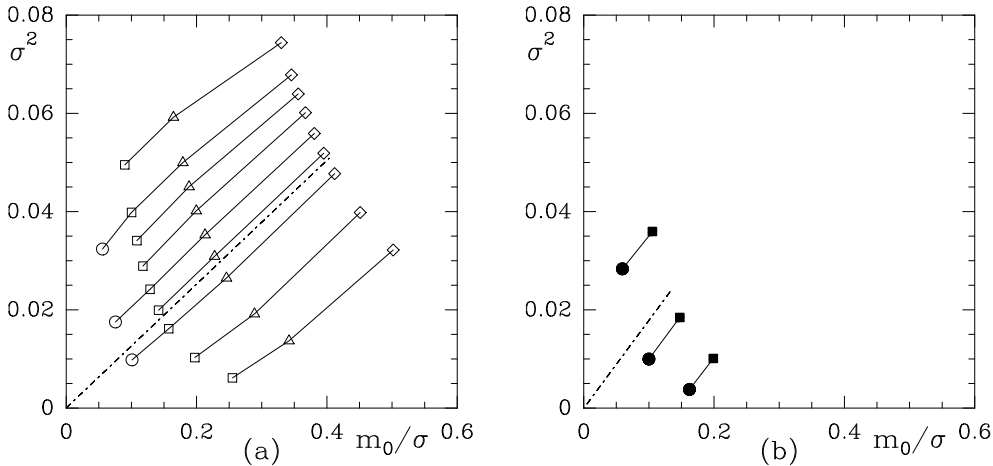


Figure 2: Fisher plots of Monte Carlo data for the chiral condensate σ on (a) $8^3 \times 16$ and (b) 12^4 lattices.

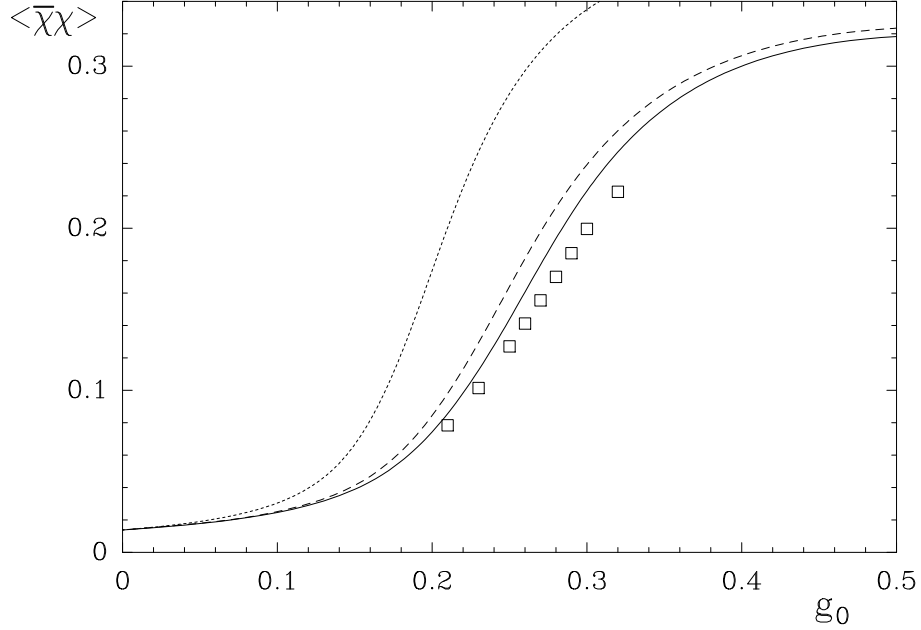


Figure 3: Comparison of Monte Carlo data ($8^3 \times 16$ lattice, $m_0 = 0.02$) for the chiral condensate with results from the gap equation (dotted line), the order g_0 (dashed line) and the order g_0^2 (solid line) Schwinger-Dyson equations.

In the gap equation this occurs at

$$g_c = \frac{1}{8y} \approx 0.201700, \quad (3.1)$$

		$\langle \bar{\chi}\chi \rangle$		
g_0	m_0	8^4	12^4	∞
0.21	0.01	0.0294(1)	0.0284(1)	0.0275(3)
0.23	0.01	0.0419(3)	0.0399(1)	0.0387(5)
0.25	0.01	0.0632(8)	0.0616(4)	0.0608(11)
	0.02	0.1044(10)	0.1005(3)	0.0992(8)
0.27	0.01	0.1039(12)	0.0999(10)	0.0986(18)
	0.02	0.1421(13)	0.1358(5)	0.1343(10)
0.28	0.01	0.1283(11)	0.1242(9)	0.1230(15)
0.30	0.01	0.1675(20)	0.1683(6)	0.1685(10)
	0.02	0.1929(12)	0.1896(4)	0.1892(6)
0.32	0.01	0.2021(11)	0.2042(7)	0.2045(9)

Table 1: Monte Carlo results for the chiral condensates on lattices with $L_s : L_t = 1 : 1$. The third column gives the extrapolation to infinite volume using eq. (3.24).

$\langle \bar{\chi}\chi \rangle$				
g_0	m_0	$6^3 \times 12$	$8^3 \times 16$	∞
0.21	0.02	0.1100(7)	0.0784(2)	0.0559(18)
	0.04	0.1458(8)	0.1170(4)	0.0963(19)
	0.09	0.1995(7)	0.1794(2)	0.1688(9)
0.23	0.02	0.1354(10)	0.1014(3)	0.0765(24)
	0.04	0.1685(5)	0.1385(4)	0.1182(17)
	0.09	0.2170(3)	0.1995(3)	0.1915(7)
0.25	0.01	0.1358(12)	0.0991(7)	0.0720(43)
	0.02	0.1604(8)	0.1271(5)	0.1034(25)
	0.04	0.1890(6)	0.1627(5)	0.1471(17)
	0.09	0.2339(6)	0.2185(3)	0.2124(8)
0.26	0.02	0.1721(7)	0.1412(6)	0.1205(27)
	0.04	0.2014(12)	0.1757(4)	0.1618(18)
	0.09	0.2426(6)	0.2278(3)	0.2224(7)
0.27	0.01	0.1592(13)	0.1324(8)	0.1139(38)
	0.02	0.1853(9)	0.1555(5)	0.1369(24)
	0.04	0.2096(8)	0.1878(5)	0.1767(16)
	0.09	0.2483(9)	0.2364(3)	0.2325(8)
0.28	0.02	0.1962(9)	0.1700(5)	0.1542(24)
	0.04	0.2197(9)	0.2004(4)	0.1915(14)
	0.09	0.2560(6)	0.2452(3)	0.2419(7)
0.29	0.02	0.2068(12)	0.1846(7)	0.1730(24)
	0.04	0.2305(8)	0.2123(3)	0.2048(10)
	0.09	0.2621(5)	0.2529(4)	0.2503(8)
0.30	0.01	0.1969(14)	0.1799(7)	0.1703(30)
	0.02	0.2169(9)	0.1996(6)	0.1919(18)
	0.04	0.2383(9)	0.2235(5)	0.2180(13)
	0.09	0.2698(6)	0.2605(3)	0.2580(6)
0.32	0.02	0.2356(10)	0.2225(6)	0.2172(17)
	0.04	0.2531(9)	0.2433(5)	0.2404(11)
	0.09	0.2798(6)	0.2728(4)	0.2711(7)

Table 2: Monte Carlo results for the chiral condensates on lattices with $L_s : L_t = 1 : 2$. The third column gives the extrapolation to infinite volume using eq. (3.24).

where

$$y = \int_0^{2\pi} \frac{d^4 k}{(2\pi)^4} \frac{1}{\sum_\mu \sin^2 k_\mu} = \int_0^\infty d\alpha e^{-2\alpha} I_0^4(\alpha/2) \approx 0.619734, \quad (3.2)$$

and in the order g_0 case at

$$g_c = \frac{32y}{(16y - 1)^2} \approx 0.249483. \quad (3.3)$$

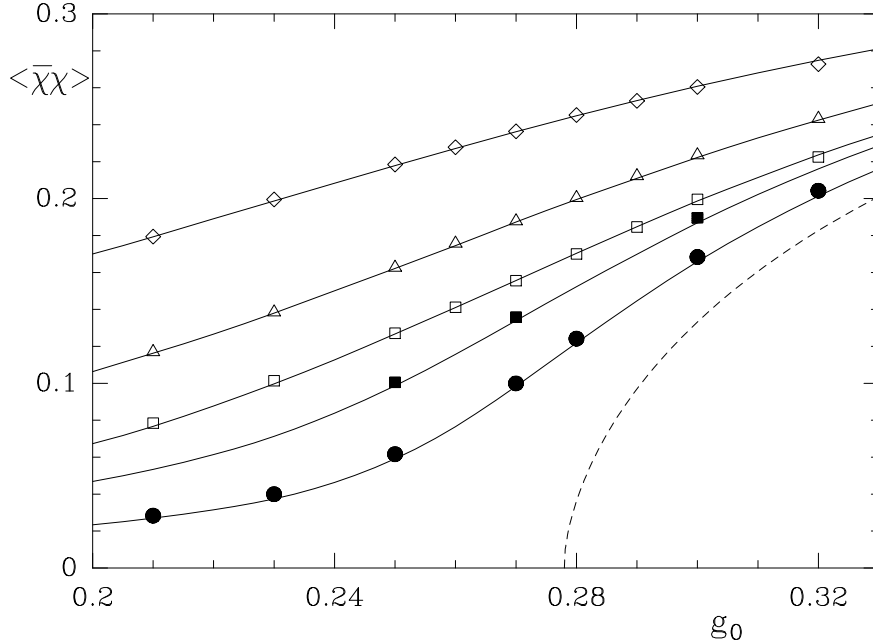


Figure 4: Monte Carlo data for the chiral condensate and curves resulting from the phenomenological fit eq. (3.4). The dashed line indicates the extrapolation to infinite volume and zero bare mass. Symbol shape denotes bare mass (diamonds 0.09, triangles 0.04, squares 0.02 and circles 0.01). Colour denotes lattices size (white $8^3 \times 16$ and black 12^4).

In the order g_0^2 case we can give no formula but the number is $g_c \approx 0.263$.

The semi-quantitative success of these equations motivated us to make a phenomenological fit to the Monte Carlo data based on a modified gap equation

$$\sigma = \frac{c_5}{V} \sum_k \frac{M}{M^2 + \sum_\mu \sin^2 k_\mu}, \quad (3.4)$$

where σ is the chiral condensate and

$$M = (c_1 + c_2 g_0 + c_3 g_0^2) \sigma + c_4 m_0. \quad (3.5)$$

The values of the parameters were found to be: $c_1 = 0.149(1)$, $c_2 = 6.37(1)$, $c_3 = -3.07(1)$, $c_4 = 0.938(1)$ and $c_5 = 0.959(1)$. The results of this fit are plotted in fig. 4 which includes data from different lattice sizes showing that the fit equation also accommodates quite nicely the finite size effects. Extrapolating the phenomenological equation to infinite volume and zero mass gives $g_c \approx 0.278$. Comparing this value with the above results gives a shift of about 0.015 relative to the order g_0^2 Schwinger-Dyson equations.

The Schwinger-Dyson equations as well as the fit equation in the infinite volume limit lead to the following scaling laws sufficiently close to the critical point:

$$\sigma^2 \ln(\sigma_0/\sigma) \propto g_0 - g_c \quad (3.6)$$

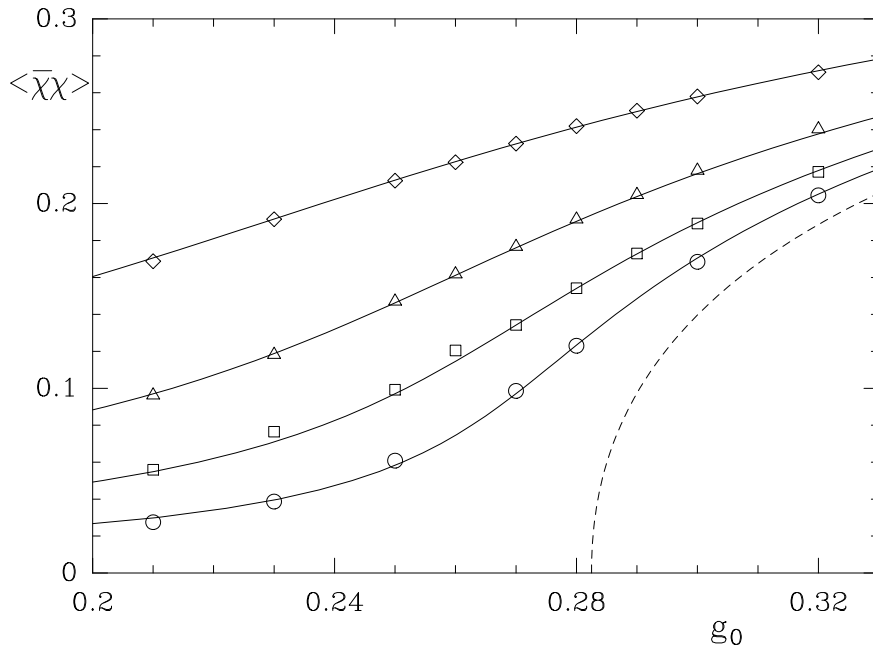


Figure 5: Monte Carlo data for the chiral condensate extrapolated to infinite volume and curves resulting from the mean-field fit with logarithmic corrections eq. (3.11). The dashed line indicates the extrapolation to zero bare mass. Symbol shape denotes bare mass (diamonds 0.09, triangles 0.04, squares 0.02 and circles 0.01).

on the critical line $m_0 = 0$ and

$$\sigma^3 \ln(\sigma_0/\sigma) \propto m_0 \quad (3.7)$$

at $g_0 = g_c$ (σ_0 is a constant of order 1). This is mean-field behaviour with logarithmic corrections. Although at this order the power of the logarithm is +1 it is possible that the inclusion of higher order Feynman diagrams could change this power.

For a more direct determination of the critical exponents and logarithmic corrections we extrapolate the data to the infinite volume first and then fit the result with a simple effective potential. The extrapolation of the chiral condensate to the infinite volume is done in section 3.3, and the results are stated in tables 1 and 2. Wherever we have two extrapolations, we take the one coming from the larger volume. We have performed two fits. In the first fit we assume an equation of state of the form

$$m_0 = \left(\delta - \frac{1}{\beta} + 1\right) \kappa \sigma^{\delta - \frac{1}{\beta}} + (\delta + 1) \zeta \sigma^\delta, \quad (3.8)$$

with

$$\kappa = \kappa_1 (g_0 - g_c), \quad (3.9)$$

$$\zeta = \zeta_0 + \zeta_1 (g_0 - g_c), \quad (3.10)$$

thus leaving the critical exponents as free parameters. We find $\kappa_1 = -3.1(1)$, $\zeta_0 = 2.6(2)$, $\zeta_1 = 8(1)$, $\beta = 0.42(1)$, $\delta = 3.4(1)$ and $g_c = 0.280(1)$. The exponents β and δ lie rather close to their mean field values (1/2 and 3 respectively). In the second fit we fix β and δ to their mean field values but allow for logarithmic corrections:

$$m_0 = 2\kappa \frac{\sigma}{\ln^p|\sigma^{-1}|} + 4\zeta \frac{\sigma^3}{\ln^q|\sigma^{-1}|}. \quad (3.11)$$

The result of the fit is $\kappa_1 = -3.6(3)$, $\zeta_0 = 2.1(3)$, $\zeta_1 = 9(2)$, $p = 0.36(11)$, $q = 0.84(1)$ and $g_c = 0.282(2)$. The data and the fit are plotted in fig. 5. (The former fit leads to similar curves.) It is pleasing to note that all three fits give roughly the same value of g_c . It is however possible that the powers p and q found from the fit eq. (3.11) have not yet reached their asymptotic values in the parameter region we have covered.

To gain a first impression of the short distance behaviour of the model we have taken our data and in fig. 6 plotted the four fermion condensate, $\sigma_4 = \frac{1}{4} \sum_{x,\mu} \langle \bar{\chi}(x)\chi(x)\bar{\chi}(x+\hat{\mu})\chi(x+\hat{\mu}) \rangle / V$, against the chiral condensate. σ_4 was also calculated via a stochastic estimator, but now involves two fermion matrix inversions. (The number of sets of random numbers used and hence inversions performed was also increased from one for the chiral condensate to $\sim O(10\%)$ of the number of molecular dynamics steps in the Hybrid Monte Carlo program.) The results are given in table 3. The points appear to lie roughly on one curve. We have compared the Monte Carlo data with the

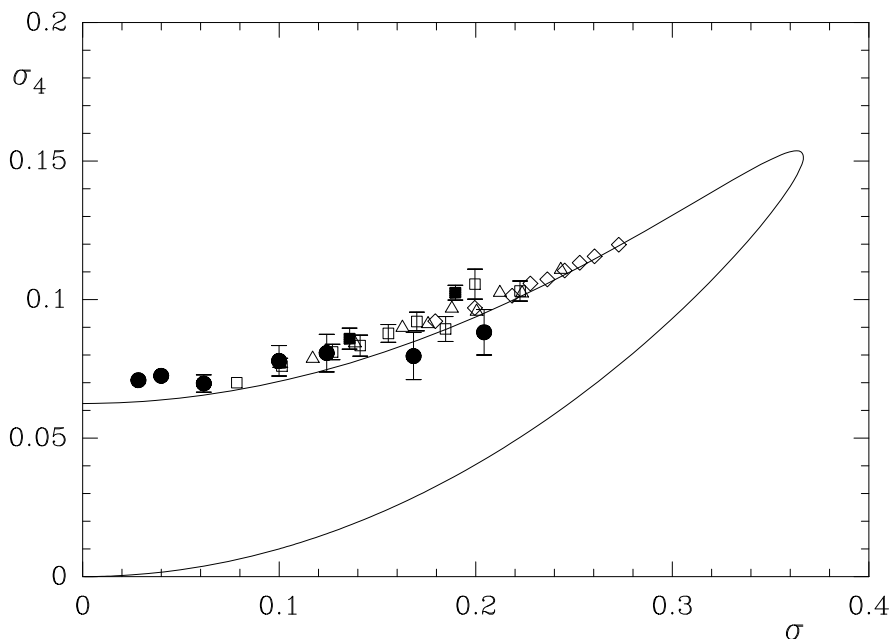


Figure 6: Monte Carlo results for the four fermion condensate plotted against the chiral condensate. The curve results from eqs. (3.12) and (3.13). The symbols are the same as in fig. 4.

σ_4					
g_0	12^4		$8^3 \times 16$		
	$m_0 = 0.01$	$m_0 = 0.02$	$m_0 = 0.02$	$m_0 = 0.04$	$m_0 = 0.09$
0.21	0.071(1)		0.070(3)	0.079(1)	0.0922(4)
0.23	0.072(2)		0.076(3)	0.084(2)	0.0970(5)
0.25	0.070(3)	0.077(2)	0.081(3)	0.090(1)	0.1014(5)
0.26			0.083(4)	0.091(1)	0.1058(6)
0.27	0.078(6)	0.086(4)	0.088(3)	0.097(2)	0.1073(5)
0.28	0.081(7)		0.092(3)	0.096(1)	0.1105(4)
0.29			0.089(4)	0.102(1)	0.1133(6)
0.30	0.080(8)	0.102(3)	0.106(5)	0.102(1)	0.1156(5)
0.32	0.088(8)		0.103(4)	0.111(3)	0.1198(6)

Table 3: Monte Carlo results for the four fermion condensate σ_4 .

naive result obtained from free fermion propagators. This gives

$$\begin{aligned} \sigma_4(m) &= \frac{1}{4} \sum_{\nu} \left[\frac{1}{V} \sum_p \frac{\sin^2 p_{\nu}}{\sum_{\lambda} \sin^2 p_{\lambda} + m^2} \right]^2 + \sigma(m)^2 \\ &\xrightarrow{V \rightarrow \infty} \frac{1}{16} [1 - m\sigma(m)]^2 + \sigma(m)^2 \end{aligned} \quad (3.12)$$

against

$$\begin{aligned} \sigma(m) &= \frac{m}{V} \sum_p \frac{1}{\sum_{\lambda} \sin^2 p_{\lambda} + m^2} \\ &\xrightarrow{V \rightarrow \infty} \int_{-\pi}^{\pi} \frac{d^4 p}{(2\pi)^4} \frac{m}{\sum_{\lambda} \sin^2 p_{\lambda} + m^2}, \end{aligned} \quad (3.13)$$

where m is to be regarded as a parameter. The infinite volume result is also plotted in fig. 6. The data lie close to the upper branch (this corresponds to small μ_R , while the lower branch corresponds to large μ_R). This similarity between the data and the free fermion formula suggests that there is only little interaction between the fermions, the main effect of the interaction being the generation of a renormalised mass, the determination of which we shall now turn to.

3.2 Fermion Propagator

To determine the fermion mass the fermion propagator

$$G(t) = \sum_{\vec{x}} \langle \chi(\vec{x}, t) \bar{\chi}(\vec{0}, 0) \rangle \quad (3.14)$$

x_1, x_2, x_3 even

is fitted by

$$G(t) = \frac{Z_2}{(1 + e^{-\mu_R L t}) \cosh \mu_R} \left(e^{-\mu_R t} - (-1)^t e^{-\mu_R(Lt-t)} \right). \quad (3.15)$$

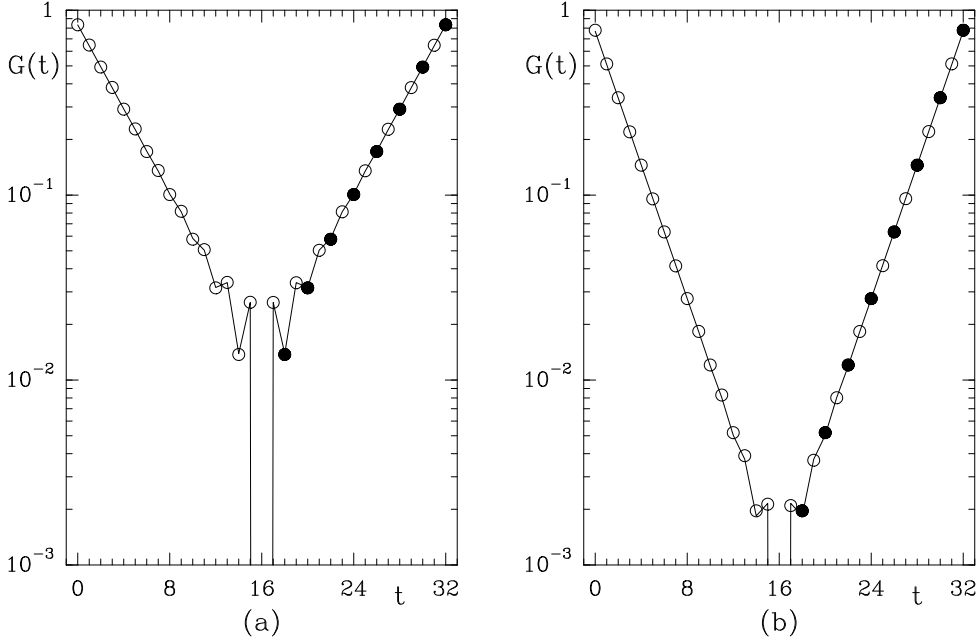


Figure 7: Fermion propagators from Monte Carlo calculations on an $8^3 \times 32$ lattice at $m_0 = 0.04$, $g_0 = 0.23$ (a) and $g_0 = 0.28$ (b). Open (solid) symbols represent positive (negative) values. The lines connect values from fits using eq. (3.15). The resulting fermion masses are (a) $\mu_R = 0.262(1)$ and (b) $\mu_R = 0.417(1)$.

The parameter μ_R is the renormalised fermion mass and Z_2 is the wave-function renormalisation constant. The results of the fits are given in tables 4, 5 and 6. In fig. 7 we show two propagators on $8^3 \times 32$ lattices which were simulated to check the masses obtained on lattices with smaller time extent.

Z_2					
g_0	12^4		$8^3 \times 16$		
	$m_0 = 0.01$	$m_0 = 0.02$	$m_0 = 0.02$	$m_0 = 0.04$	$m_0 = 0.09$
0.21	0.872(1)		0.865(1)	0.872(1)	0.887(1)
0.23	0.857(1)		0.858(2)	0.867(2)	0.880(1)
0.25	0.834(1)	0.848(1)	0.842(2)	0.858(2)	0.871(2)
0.26				0.854(2)	0.865(2)
0.27	0.825(2)	0.830(2)	0.835(3)	0.847(2)	0.866(2)
0.28	0.817(2)		0.836(3)	0.845(2)	0.865(2)
0.29			0.831(3)	0.845(1)	0.860(2)
0.30	0.816(3)	0.832(2)	0.832(3)	0.848(4)	0.862(2)
0.32	0.827(3)		0.825(4)	0.844(3)	0.853(3)

Table 4: Monte Carlo results for the wave-function renormalisation constant Z_2 .

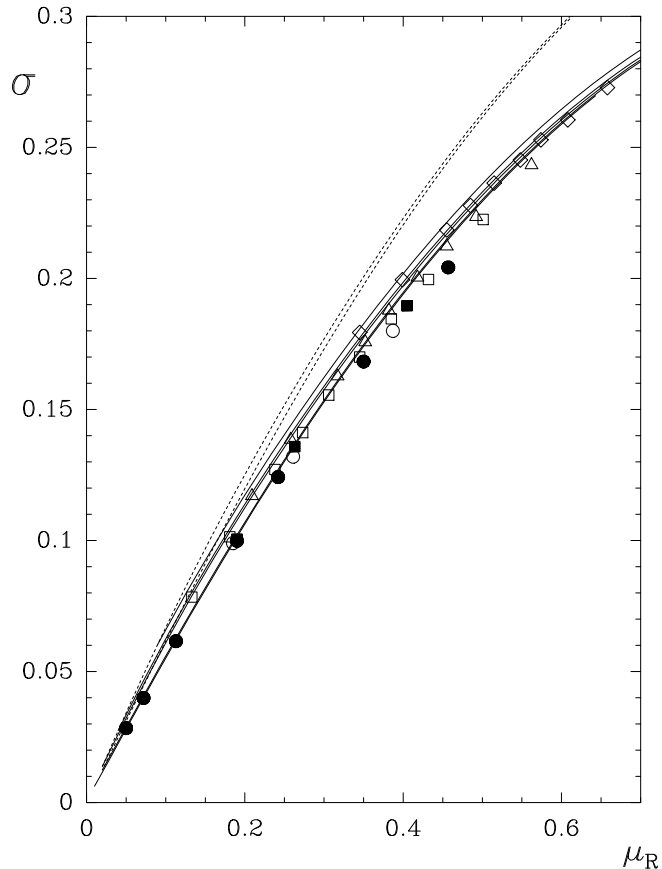


Figure 8: Monte Carlo results for the chiral condensate plotted versus the renormalised fermion mass. The dotted lines are results from the gap equation. The solid lines are results from the order g_0^2 Schwinger-Dyson equations. The symbols are the same as in fig. 4.

We see that their behaviour is very well described by a single exponential.

In fig. 8 we plot $\langle \bar{\chi}\chi \rangle$ against μ_R . In this plot we have also shown the predictions of the gap equation and of the order g_0^2 Schwinger-Dyson equations. We see that the data lie in a narrow band. The theoretical curves also display a small width because they still have weak dependences on bare mass and lattice size. The small spread tells us that the form of the fermion propagator is hardly changed by the interactions.

3.3 Finite Size Effects

Comparing results found on lattices with different volumes (see tables 1 and 2) makes it clear that we have large finite size effects in our data, and that it is important to study these in order to see the picture for an infinite lattice. An advantage we have over the usual situation in a Monte Carlo calculation is that we can use the Schwinger-Dyson equations to calculate re-

		μ_R		
g_0	m_0	8^4	12^4	∞
0.21	0.01	0.051(0)	0.050(0)	0.050(1)
0.23	0.01	0.075(1)	0.072(0)	0.070(1)
0.25	0.01	0.116(1)	0.113(0)	0.112(2)
	0.02	0.196(2)	0.190(0)	0.188(1)
0.27	0.01	0.202(3)	0.190(1)	0.185(3)
	0.02	0.274(2)	0.263(1)	0.260(2)
0.28	0.01	0.258(3)	0.242(1)	0.237(2)
0.30	0.01	0.352(4)	0.350(1)	0.350(2)
	0.02	0.412(3)	0.405(1)	0.404(2)
0.32	0.01	0.460(6)	0.457(2)	0.456(2)

Table 5: *Monte Carlo results for the renormalised fermion mass on lattices with $L_s : L_t = 1 : 1$. The third column gives the extrapolation to infinite volume using eq. (3.23).*

sults on large or even on infinite lattices, and so see how the thermodynamic limit is approached.

To keep the calculations reasonably simple we will look at the lattice size dependence of the solutions of the order g_0 Schwinger-Dyson equations (2.14), but we expect that the form of the formulae found will remain true in general.

The equations (2.14) always involve the sum over allowed momenta of some function $a(k)$ of the momentum. Let us call such a sum U_a . We need to compare this sum over momenta with the integral over all momenta which gives the infinite volume limit. We do this by using the Poisson resummation formula to rewrite our sum as an integral

$$\begin{aligned}
U_a &= \frac{1}{V} \sum_k a(k) \\
&= \int d^4k' \frac{1}{V} \sum_k a(k') \delta(k' - k).
\end{aligned} \tag{3.16}$$

The sum of δ functions can be expressed as a Fourier series, leading to

$$U_a = \sum_n (-1)^{n_t} A(\vec{n}L_s, n_tL_t), \tag{3.17}$$

where A is the Fourier transform of a defined by

$$A(x) = \int \frac{d^4k}{(2\pi)^4} e^{ik \cdot x} a(k) \tag{3.18}$$

(the $(-1)^{n_t}$ arises because of the antiperiodic boundary conditions in time). The functions that we consider will always have Fourier transforms which decrease exponentially at large distance. Therefore in an infinite volume only

		μ_R		
g_0	m_0	$6^3 \times 12$	$8^3 \times 16$	∞
0.21	0.02	0.183(1)	0.133(0)	0.098(3)
	0.04	0.250(1)	0.209(0)	0.179(2)
	0.09	0.377(1)	0.345(0)	0.328(1)
0.23	0.02	0.240(2)	0.181(0)	0.138(4)
	0.04	0.311(1)	0.258(0)	0.222(3)
	0.09	0.430(1)	0.399(0)	0.385(1)
0.25	0.01	0.268(3)	0.185(1)	0.123(8)
	0.02	0.305(2)	0.238(1)	0.191(4)
	0.04	0.364(2)	0.317(1)	0.289(3)
	0.09	0.483(1)	0.455(1)	0.445(2)
0.26	0.02	0.334(2)	0.273(1)	0.232(6)
	0.04	0.397(2)	0.352(1)	0.328(3)
	0.09	0.512(1)	0.485(1)	0.475(2)
0.27	0.01	0.329(3)	0.261(1)	0.213(8)
	0.02	0.365(2)	0.306(1)	0.269(5)
	0.04	0.430(2)	0.382(1)	0.358(3)
	0.09	0.538(1)	0.515(1)	0.508(2)
0.28	0.02	0.416(3)	0.345(1)	0.303(6)
	0.04	0.462(2)	0.418(1)	0.398(3)
	0.09	0.572(2)	0.548(1)	0.541(2)
0.29	0.02	0.442(3)	0.385(1)	0.355(6)
	0.04	0.492(2)	0.455(1)	0.440(2)
	0.09	0.593(2)	0.574(1)	0.569(2)
0.30	0.01	0.463(5)	0.387(2)	0.343(10)
	0.02	0.476(3)	0.432(1)	0.412(5)
	0.04	0.534(3)	0.492(2)	0.477(4)
	0.09	0.630(2)	0.608(1)	0.602(2)
0.32	0.02	0.563(5)	0.501(2)	0.475(7)
	0.04	0.585(3)	0.562(1)	0.555(3)
	0.09	0.681(2)	0.658(1)	0.653(2)

Table 6: Monte Carlo results for the renormalised fermion mass on lattices with $L_s : L_t = 1 : 2$. The third column gives the extrapolation to infinite volume using eq. (3.23).

$A(0)$ survives, while on a large lattice the finite size effects will be dominated by terms where one of the n_μ is ± 1 . Physically speaking these represent the contributions of particles which have travelled “once around the lattice”. Terms where two of the n_μ ’s are non-zero, or one of the n_μ ’s is larger than 1 die away as exponentials with higher exponent than the leading correction and very quickly become negligible.

To see what the finite size corrections to the fermion propagator are we

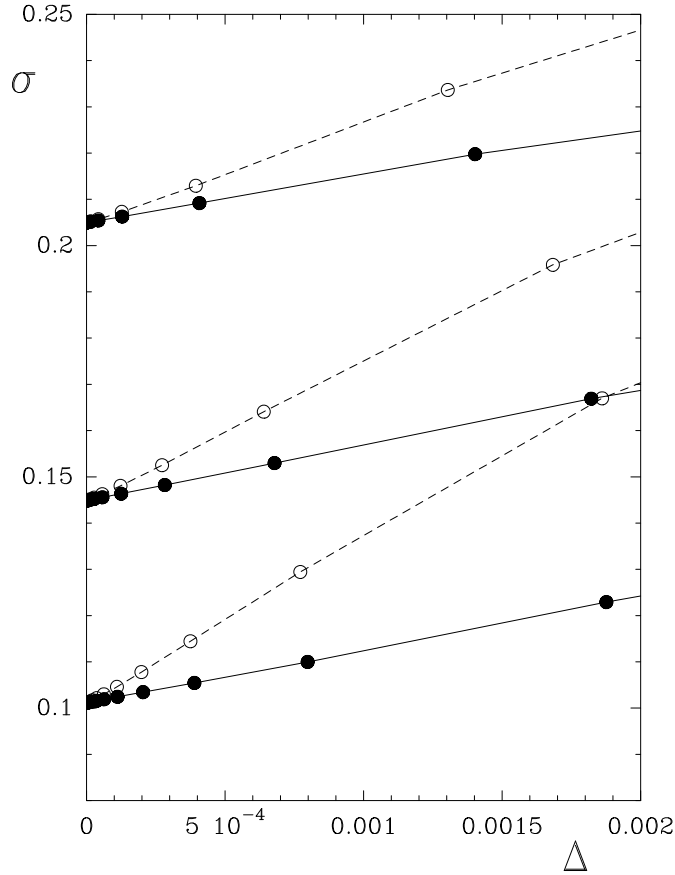


Figure 9: *Finite size scaling of the chiral condensate. Plotted are Schwinger-Dyson results on lattices with $L_s \geq 6$; $L_s : L_t = 1 : 1$ (solid symbols) and $L_s : L_t = 1 : 2$ (open symbols). The parameters are $m_0 = 0.02$ and $g_0 = 0.23, 0.25, 0.28$.*

need to know the large distance behaviour of the Fourier transforms of

$$\frac{N}{N^2 + \sum_{\nu} F_{\nu}^2 \sin^2 k_{\nu}} \quad (3.19)$$

and

$$\frac{F_{\mu} \sin^2 k_{\mu}}{N^2 + \sum_{\nu} F_{\nu}^2 \sin^2 k_{\nu}}, \quad (3.20)$$

i. e., the large distance behaviour of the fermion propagator. These limits can be found by the saddle point approximation. For definiteness we look at the case $n_1 = 1$. First integrate over k_1 which can be done exactly by looking at residues at the poles of the integrand:

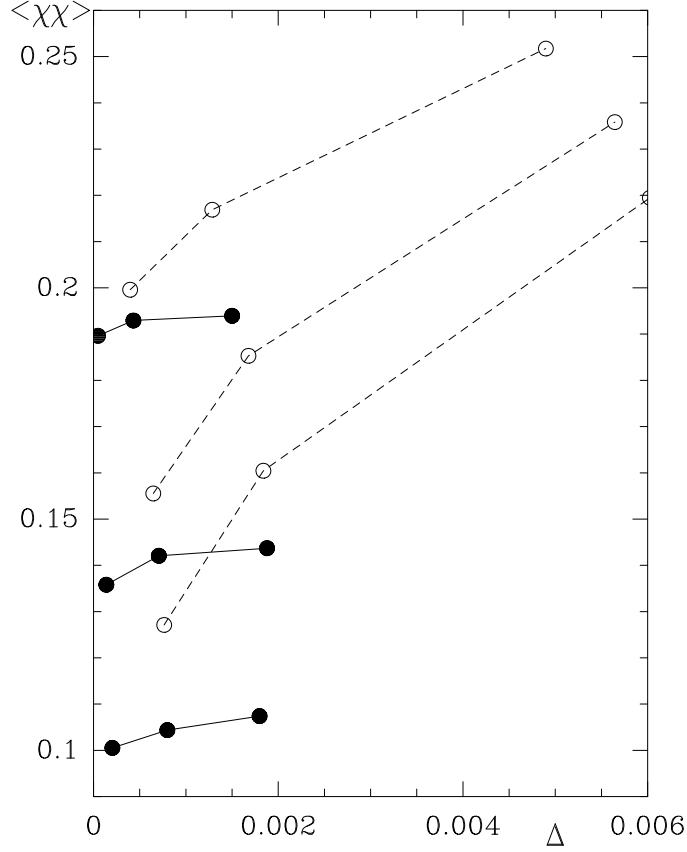


Figure 10: *Finite size scaling of the chiral condensate (Monte Carlo results).* The lattice sizes are 6^4 , 8^4 and 12^4 (\bullet) and $4^3 \times 8$, $6^3 \times 12$ and $8^3 \times 16$ (\circ). The parameters are $m_0 = 0.02$ and $g_0 = 0.25, 0.27, 0.30$.

$$\begin{aligned}
& \int \frac{d^4k}{(2\pi)^4} \exp(ik_1 L_s) \frac{N}{N^2 + \sum_{\nu} F_{\nu}^2 \sin^2 k_{\nu}} \\
L_s \equiv & \int \frac{dk_2 dk_3 dk_4}{(2\pi)^3} \frac{1}{\sqrt{N^2 + \sum_{\nu \neq 1} F_{\nu}^2 \sin^2 k_{\nu}}} \frac{N}{\sqrt{N^2 + F_1^2 + \sum_{\nu \neq 1} F_{\nu}^2 \sin^2 k_{\nu}}} \\
& \times \exp \left[-L_s \sinh^{-1} \left(\frac{\sqrt{N^2 + \sum_{\nu \neq 1} F_{\nu}^2 \sin^2 k_{\nu}}}{F_1} \right) \right]. \quad (3.21)
\end{aligned}$$

For large L_s this integral is dominated by $\sin k_{\nu} \approx 0$ and is approximately Gaussian:

$$\begin{aligned}
& \approx \left(\frac{2N}{\pi L_s} \right)^{\frac{3}{2}} \frac{(N^2 + F_1^2)^{1/4}}{F_2 F_3 F_4} \exp \left[-L_s \sinh^{-1}(N/F_1) \right] \\
& \propto (\mu_R/L_s)^{\frac{3}{2}} \exp(-\mu_R L_s). \quad (3.22)
\end{aligned}$$

(In the final expression $\mu_R \ll 1$ has been taken.) The change in the sum for eq. (3.20) also has the same L_s dependence. The propagators in the 2- and 3- direction have the same form. In the 4-direction L_s goes to L_t .

Naturally the eigenvalues of the transfer matrix are independent of the temporal extension of the lattice, nevertheless the rate at which correlation functions decay can depend on L_t , and it is this decay rate which is used to measure μ_R at finite L_t . The infinite volume limit turns out to be independent of L_t/L_s .

The change in the solution of (2.14) will be proportional to the difference between the finite volume sum and the infinite volume integral when this difference is itself small. This leads to the expectation that for $L_t \geq L_s$

$$\mu_R - \mu_R(\infty) \propto g_0(\mu_R/L_s)^{\frac{3}{2}} \exp(-\mu_R L_s) \quad (3.23)$$

and

$$\langle \bar{\chi}\chi \rangle - \langle \bar{\chi}\chi \rangle(\infty) \propto (\mu_R/L_s)^{\frac{3}{2}} \exp(-\mu_R L_s) \equiv \Delta. \quad (3.24)$$

These equations are to be understood as giving the form of the L_s dependence at fixed bare parameters for large L_s . The constant of proportionality depends on the values of the bare parameters.

The above predictions have been tested by plotting $\langle \bar{\chi}\chi \rangle$ or μ_R against the right-hand side of (3.23), (3.24) respectively. Data for a given lattice shape should fall on a straight line. In fig. 9 we show the Schwinger-Dyson results for the chiral condensate and see that the asymptotic formula (3.24) holds for $L_s \geq 6$. A similar conclusion holds for the Monte Carlo results as fig. 10 reveals. We gain added faith in this extrapolation to infinite volume from the fact that lattices with $L_t = L_s$ and with $L_t = 2L_s$ both extrapolate to the same value at infinite volumes. The extrapolated values for $\langle \bar{\chi}\chi \rangle$ and μ_R are given in tables 1, 2, 5 and 6. It is pleasing to note that the results from the 12^4 lattice already lie very close to the infinite volume results.

The above formulae are only valid in a domain where *any* $mass \times L_s$ is large. Near the critical line $m_\pi \times L_s$ is very small and the finite size formulae of [20] should apply. Near the critical point *all* $masses \times L_s$ are very small and the exponential corrections turn into power law corrections.

4 Fermion-Antifermion Composite States

We now turn to the determination of the energies of fermion-antifermion composite states (“mesons”).

4.1 Monte Carlo Method

We calculated the correlation functions of bilinear operators of definite lattice symmetry which are well known from QCD spectroscopy (see, e. g., [21, 22]). We looked at four local operators and a one bond operator. For results on other one bond operators see [14]. The propagators for the local-local correlation functions have been calculated with 48 sources. Additionally we considered four wall operators [23]. The local operators $\mathcal{O}^{(0)}$ are given by

$$\mathcal{O}_{i,k}^{(0)}(t) = \sum_{\vec{x}} s_{i,k}(\vec{x}, t) \bar{\chi}(\vec{x}, t) \chi(\vec{x}, t), \quad (4.1)$$

where the s factors and the corresponding continuum quantum number assignments are given in the table 7. The notation for the continuum quantum numbers is the standard J^{PC} . The subscript is the $SU(4)$ flavour representation (a for adjoint, s for singlet) under the assumption that the $SU(4)$ flavour symmetry is restored. Our fifth operator is

$$\mathcal{O}_{1,k}^{(1)}(t) = \frac{1}{2} \sum_{\vec{x}} \eta_k(\vec{x}, t) \bar{\chi}(\vec{x}, t) [\chi(\vec{x} + \hat{k}, t) + \chi(\vec{x} - \hat{k}, t)]. \quad (4.2)$$

For the wall operators we take

$$\mathcal{O}_{i,k}^{(w)}(t) = \left(\frac{2}{L_s}\right)^3 \sum_{\vec{x}, \vec{e}} s_{i,k}(\vec{x}, t) \bar{\chi}(\vec{x} + \vec{e}, t) \chi(\vec{x}, t). \quad (4.3)$$

i	$s_{i,k}(\vec{x}, t)$	J^{PC}	name	J^{PC}	name
local operators					
1	$(-1)^t$	0_a^{-+}	π'	0_s^{++}	σ
2	$(-1)^{x_1+x_2+x_3+t}$	0_a^{-+}	π	0_a^{+-}	–
3	$(-1)^{x_k+t}$	1_a^{--}	ρ'	1_a^{++}	a
4	$(-1)^{x_1+x_2+x_3-x_k+t}$	1_a^{--}	ρ	1_a^{+-}	b
one-bond operator					
	$\eta_k(\vec{x}, t)$	1_s^{--}	ω	1_a^{+-}	b'
terms in eq. (4.11):		E^+		E^-	

Table 7: Sign factors, corresponding continuum quantum number assignments and names of the particles that are used in the text. The last line gives the connection to the fit function, eq. (4.11).

The \vec{e} sum extends over the vectors with all coordinates even. Correlation functions are

$$C_i^{(l)}(t) = \langle \mathcal{O}_{i,k}^{(l)}(t) \mathcal{O}_{i,k}^{(l)}(0) \rangle - \langle \mathcal{O}_{i,k}^{(l)}(t) \rangle \langle \mathcal{O}_{i,k}^{(l)}(0) \rangle, \quad l = 0, 1, \quad (4.4)$$

$$C_i^{(w)}(t) = \langle \mathcal{O}_{i,k}^{(0)}(t) \mathcal{O}_{i,k}^{(w)}(0) \rangle - \langle \mathcal{O}_{i,k}^{(0)}(t) \rangle \langle \mathcal{O}_{i,k}^{(w)}(0) \rangle. \quad (4.5)$$

They are independent of k . Whenever several values of k are possible we averaged over them.

These correlation functions are the sum of a fermion line connected and a fermion line disconnected part (annihilation part). Pictorially this is represented as

$$C = \left\langle \begin{array}{c} \bullet \quad \bullet \\ \curvearrowright \end{array} \right\rangle + \left\langle \begin{array}{c} \bullet \quad \bullet \\ \curvearrowright \quad \curvearrowright \end{array} \right\rangle - \left\langle \begin{array}{c} \bullet \\ \curvearrowright \end{array} \right\rangle \left\langle \begin{array}{c} \bullet \\ \curvearrowright \end{array} \right\rangle, \quad (4.6)$$

where the brackets indicate averaging over the auxiliary field. Usually one measures only the fermion line connected part which is the first term in (4.6). The second term, which we call the annihilation part, is computationally very demanding because the noise problem is more severe. However we have also attempted to measure the annihilation part with a stochastic estimator. The last term only contributes for particles with vacuum quantum numbers.

Let us now turn to the discussion of our fit formulae. By means of a complete set of eigenstates of the transfer matrix one can write

$$\begin{aligned} C(t) &= \langle \mathcal{O}(t) \mathcal{O}'(0) \rangle \\ &= \sum_{i,j} \langle i | \hat{\mathcal{O}} | j \rangle \langle j | \hat{\mathcal{O}}' | i \rangle e^{-E_j t - E_i(L_t - t)} \sigma_j^t \sigma_i^{L_t - t}, \end{aligned} \quad (4.7)$$

with $\sigma_i = \pm 1$. For a more detailed discussion of the $\hat{\mathcal{O}}$ and the σ_i see [22]. If L_t was infinite one of the intermediate states in the sum would always be the vacuum, but on a finite lattice we have a genuine double sum. Terms will occur in the sum where $E_i = E_j$ which contribute either a constant or an ‘‘oscillating constant’’ depending on whether σ_i and σ_j have the same or opposite sign. (The reader may at first be surprised to hear that there are states with identical energy but opposite σ . In the fermionic sector there are several discrete symmetries which change σ but leave E unchanged. For example the action (2.2) is invariant under the transformation

$$\chi(x) \rightarrow \zeta_\mu(x) \chi(x + \hat{\mu}), \quad \bar{\chi}(x) \rightarrow \zeta_\mu(x) \bar{\chi}(x + \hat{\mu}), \quad (4.8)$$

where

$$\zeta_\mu(x) = (-1)^{x_{\mu+1} + \dots + x_4}, \quad \zeta_4(x) = 1. \quad (4.9)$$

This transformation changes σ if μ is spacelike. Such pairs occur in the fermionic sector because of the well-known phenomenon of doubling. The propagator for staggered fermions has sixteen states instead of the four states of the continuum propagator. Eight of these states come from poles with p_4 near 0, and so correspond to ordinary exponentials in position space, the

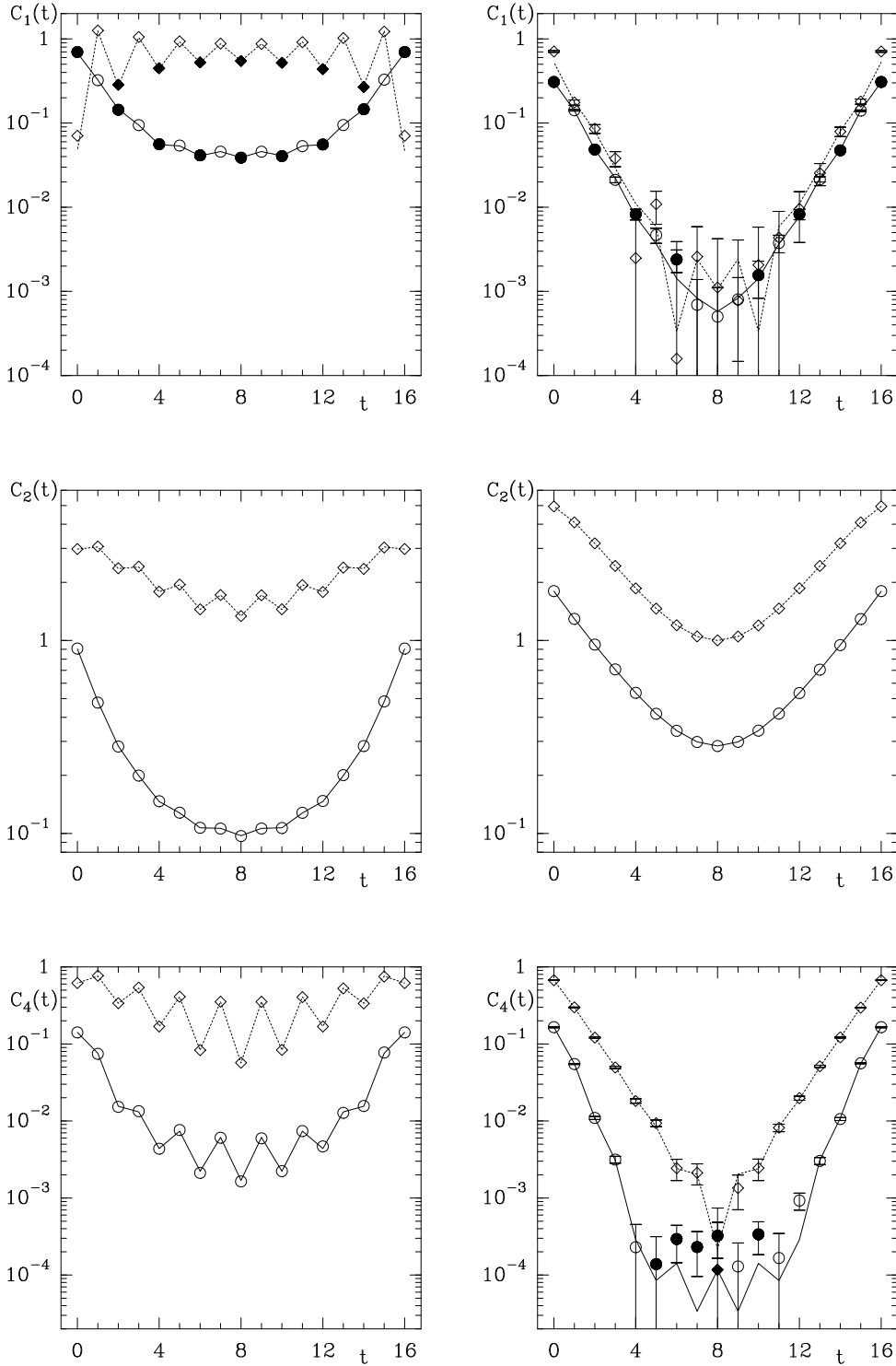




Figure 11: Meson propagators $C_i(t)$ from Monte Carlo calculations on an $8^3 \times 16$ lattice at $m_0 = 0.02$ and $g_0 = 0.21$ (l.h.s.), $g_0 = 0.32$ (r.h.s.). Shown are the local-local propagators $C_i^{(0)}(t)$ (circles) and the wall-local propagators $C_i^{(w)}(t)$ (diamonds). Open (solid) symbols represent positive (negative) values. The lines connect values from simultaneous fits using eq. (4.11).

$E_\pi^{(0)}$					
g_0	12^4		$8^3 \times 16$		
	$m_0 = 0.01$	$m_0 = 0.02$	$m_0 = 0.02$	$m_0 = 0.04$	$m_0 = 0.09$
0.21	0.095(4)		0.191(1)	0.326(1)	0.582(1)
0.23	0.129(4)		0.238(1)	0.377(1)	
0.25	0.179(4)	0.298(2)	0.280(1)	0.420(1)	
0.26			0.297(1)	0.434(1)	
0.27	0.238(5)	0.344(3)	0.310(1)	0.442(1)	0.653(1)
0.28	0.250(3)		0.317(1)	0.445(1)	
0.29			0.319(1)	0.444(1)	0.644(1)
0.30	0.244(2)	0.334(2)	0.317(1)	0.442(1)	0.638(1)
0.32	0.232(1)		0.311(1)	0.431(1)	0.624(1)

$E_\pi^{(1)}$					
g_0	12^4		$8^3 \times 16$		
	$m_0 = 0.01$	$m_0 = 0.02$	$m_0 = 0.02$	$m_0 = 0.04$	$m_0 = 0.09$
0.21	0.772(5)		0.880(7)	0.923(6)	1.024(5)
0.23	0.678(7)		0.828(10)	0.885(8)	
0.25	0.594(11)	0.646(8)	0.807(10)	0.889(16)	
0.26			0.816(14)	0.885(11)	
0.27	0.570(24)	0.669(13)	0.831(21)	0.947(20)	1.124(15)
0.28	0.635(20)		0.866(21)	0.974(15)	
0.29			0.902(27)	1.014(11)	1.232(15)
0.30	0.800(27)	0.885(32)	0.974(33)	1.064(15)	1.273(21)
0.32	0.953(40)		1.096(35)	1.201(33)	1.375(22)

Table 8: *Monte Carlo results for the energies of the ground state of the π particle $E_\pi^{(0)}$ and the first excited state $E_\pi^{(1)}$.*

other eight have p_4 near to π and therefore give rise to oscillating exponentials. The above symmetries ensure that the decay rate of the normal exponentials and the oscillating exponentials remains the same, even in the presence of interactions. Therefore we know that every single fermion state has a partner state with the same energy but opposite σ , so there will indeed be contributions of the “oscillating constant” type in the meson propagator. We have already come across a pair of states with the same energy but opposite σ in the fermion propagator eq. (3.15), fig. 7. The reader can easily check that at small t the propagator $G(t)$ is dominated by a normal exponential and at large t by an oscillating, but that in both cases the energy is the same.) Consider two processes contributing to the correlation functions:

- (a)  : The intermediate state is a fermion-antifermion pair,
- (b)  : A single fermion propagates around the lattice.

It is process (b) which gives rise to the constants. This can already be

checked for the free case on a finite lattice. The check is easiest for the wall propagator $C_i^{(w)}$ which in the free theory is simply the square of the fermion propagator $G(t)$ (see eq. (3.15))

$$C_{\text{free}}^{(w)}(t) = G_{\text{free}}^2(t) \propto e^{-2\mu_{\text{R}}t} + e^{-2\mu_{\text{R}}(L_t-t)} - 2(-1)^t e^{-\mu_{\text{R}}L_t} \quad (4.10)$$

which already displays an oscillating constant contribution.

From eq. (4.7) $C(t)$ thus has the form

$$\begin{aligned} C(t) &= \sum_n A_n^+ \left(e^{-E_n^+ t} + e^{-E_n^+(L_t-t)} \right) \\ &+ \sum_n A_n^- \left(e^{-E_n^- t} + e^{-E_n^-(L_t-t)} \right) (-1)^t \\ &+ B^+ \\ &+ B^- (-1)^t. \end{aligned} \quad (4.11)$$

The E^+ terms describe s -wave states and the E^- terms describe the parity partners of these states which are p -waves. The quantum numbers are given in table 7. In the following the energies are called $E_{\text{name}}^{(i)}$ where “name” is the particle name from table 7 and $i = 0$ or 1 for the energies of the ground state or first excited state.

In fitting we had to restrict ourselves to the lightest states. We used two s -wave states for the π and one s - and one p -wave state for the π'/σ . For all vector channels (ρ'/a , ρ/b , ω/b') we used two s -wave states and one p -wave state. The choices of the terms in the fit function were necessary to obtain good fits. In the case of the π correlation function it is further motivated by the fact that a 0^{+-} state cannot be realised as a fermion-antifermion state. In the other cases we were guided by the results from the Schwinger-Dyson equations. It was found that B^+ was always negligible and that B^- was necessary to describe propagators in the symmetric phase. In order to extract a maximum of information from our correlation functions we found it convenient to make a simultaneous fit to both the local-local and the wall-local correlation functions.

From the π ground state energy $E_{\pi}^{(0)}$ and amplitude $A_{\pi}^{(0)}$ we calculated the pion decay constant f_{π} using [25]:

$$f_{\pi} = \frac{m_0}{4} \sqrt{|A_{\pi}^{(0)}|} \frac{\sqrt{\sinh E_{\pi}^{(0)}}}{\sinh^2(E_{\pi}^{(0)}/2)}. \quad (4.12)$$

The fit results are given in tables 8–13. As we have seen for the chiral condensate the finite size effects are quite large. In fig. 11 we show propagators and fits of the π'/σ , π and ρ/b (top to bottom) for one g_0 -value in the symmetric and one g_0 -value in the broken phase.

f_π					
g_0	12^4		$8^3 \times 16$		
	$m_0 = 0.01$	$m_0 = 0.02$	$m_0 = 0.02$	$m_0 = 0.04$	$m_0 = 0.09$
0.21	0.073(5)		0.115(1)	0.107(1)	0.109(0)
0.23	0.070(3)		0.111(1)	0.110(1)	
0.25	0.071(3)	0.076(1)	0.112(1)	0.116(1)	
0.26			0.116(1)	0.124(1)	
0.27	0.084(3)	0.095(1)	0.120(1)	0.128(1)	0.147(1)
0.28	0.096(2)		0.126(1)	0.135(1)	
0.29			0.131(1)	0.141(0)	0.160(0)
0.30	0.119(1)	0.129(2)	0.139(1)	0.147(1)	0.164(1)
0.32	0.141(1)		0.151(1)	0.160(1)	0.173(0)

Table 9: Monte Carlo results for the pion decay constant f_π .

$E_{\pi'}^{(0)}$					
g_0	12^4		$8^3 \times 16$		
	$m_0 = 0.01$	$m_0 = 0.02$	$m_0 = 0.02$	$m_0 = 0.04$	$m_0 = 0.09$
0.21	0.100(7)		0.272(4)	0.430(3)	0.705(2)
0.23	0.145(7)		0.361(9)	0.522(6)	
0.25	0.227(9)	0.380(5)	0.483(12)	0.645(8)	
0.26			0.541(17)	0.687(9)	
0.27	0.377(22)	0.529(15)	0.617(19)	0.789(13)	1.032(8)
0.28	0.501(25)		0.675(26)	0.830(15)	
0.29			0.747(33)	0.907(11)	1.130(12)
0.30	0.683(53)	0.783(25)	0.796(44)	0.981(28)	1.223(16)
0.32	0.892(110)		0.934(72)	1.131(45)	1.303(24)

$E_\sigma^{(0)}$					
g_0	12^4		$8^3 \times 16$		
	$m_0 = 0.01$	$m_0 = 0.02$	$m_0 = 0.02$	$m_0 = 0.04$	$m_0 = 0.09$
0.21	0.751(8)		0.877(6)	0.939(4)	1.105(3)
0.23	0.665(9)		0.817(6)	0.922(4)	
0.25	0.595(11)	0.680(6)	0.811(5)	0.936(9)	
0.26			0.816(7)	0.940(5)	
0.27	0.598(17)	0.705(11)	0.824(11)	0.974(12)	1.206(10)
0.28	0.656(15)		0.855(11)	0.996(8)	
0.29			0.854(14)	1.026(6)	1.271(9)
0.30	0.771(25)	0.873(15)	0.880(17)	1.049(23)	1.300(19)
0.32	0.898(47)		0.926(29)	1.152(21)	1.364(17)

Table 10: Monte Carlo results for the energies of ground state of the π' particle $E_{\pi'}^{(0)}$ and the ground state energy of the σ particle $E_\sigma^{(0)}$.

$E_\rho^{(0)}$					
g_0	12^4		$8^3 \times 16$		
	$m_0 = 0.01$	$m_0 = 0.02$	$m_0 = 0.02$	$m_0 = 0.04$	$m_0 = 0.09$
0.21	0.101(2)		0.253(1)	0.407(1)	0.678(1)
0.23	0.144(2)		0.344(2)	0.499(2)	
0.25	0.227(3)	0.371(2)	0.460(3)	0.620(2)	
0.26			0.526(4)	0.677(3)	
0.27	0.374(5)	0.521(4)	0.595(5)	0.749(4)	0.992(4)
0.28	0.485(5)		0.662(7)	0.817(6)	
0.29			0.741(9)	0.883(4)	1.111(5)
0.30	0.676(11)	0.776(7)	0.829(13)	0.935(11)	1.187(11)
0.32	0.890(29)		0.969(43)	1.076(17)	1.290(19)

$E_\rho^{(1)}$					
g_0	12^4		$8^3 \times 16$		
	$m_0 = 0.01$	$m_0 = 0.02$	$m_0 = 0.02$	$m_0 = 0.04$	$m_0 = 0.09$
0.21	1.36(1)		1.40(2)	1.46(2)	1.54(1)
0.23	1.34(1)		1.42(2)	1.48(2)	
0.25	1.30(2)	1.35(1)	1.47(2)	1.47(4)	
0.26			1.38(3)	1.43(2)	
0.27	1.34(4)	1.34(3)	1.39(4)	1.61(7)	1.56(3)
0.28	1.52(7)		1.52(7)	1.44(3)	
0.29			1.42(6)	1.43(2)	1.57(3)
0.30	1.57(11)	1.46(5)	1.52(9)	1.51(10)	1.58(6)
0.32	1.32(10)		1.21(9)	1.60(10)	1.53(5)

$E_b^{(0)}$					
g_0	12^4		$8^3 \times 16$		
	$m_0 = 0.01$	$m_0 = 0.02$	$m_0 = 0.02$	$m_0 = 0.04$	$m_0 = 0.09$
0.21	1.41(3)		1.49(5)	1.65(5)	1.73(3)
0.23	1.42(4)		1.48(6)	1.69(6)	
0.25	1.35(5)	1.46(4)	1.63(7)	1.64(11)	
0.26			1.52(8)	1.63(6)	
0.27	1.53(15)	1.40(10)	1.51(13)	1.97(20)	1.77(11)
0.28	1.98(24)		1.97(22)	1.66(9)	
0.29			1.55(15)	1.62(6)	1.75(8)
0.30	1.90(31)	1.60(13)	1.72(21)	1.99(34)	1.77(14)
0.32	1.23(19)		1.45(21)	2.11(29)	1.82(11)

Table 11: Monte Carlo results for the energies of the ground state of the ρ particle $E_\rho^{(0)}$, its first excited state $E_\rho^{(1)}$ and the ground state of the b particle $E_b^{(0)}$.

$E_{\rho'}^{(0)}$					
g_0	12^4		$8^3 \times 16$		
	$m_0 = 0.01$	$m_0 = 0.02$	$m_0 = 0.02$	$m_0 = 0.04$	$m_0 = 0.09$
0.21	0.100(2)		0.263(2)	0.418(2)	0.692(2)
0.23	0.140(2)		0.352(3)	0.509(3)	
0.25	0.224(3)	0.374(2)	0.470(4)	0.633(3)	
0.26			0.534(5)	0.688(4)	
0.27	0.380(6)	0.519(5)	0.608(7)	0.770(5)	1.016(5)
0.28	0.490(7)		0.680(10)	0.830(7)	
0.29			0.767(12)	0.904(5)	1.141(7)
0.30	0.685(14)	0.784(10)	0.837(16)	0.943(12)	1.214(13)
0.32	0.840(25)		0.930(31)	1.099(17)	1.282(11)

$E_{\rho'}^{(1)}$					
g_0	12^4		$8^3 \times 16$		
	$m_0 = 0.01$	$m_0 = 0.02$	$m_0 = 0.02$	$m_0 = 0.04$	$m_0 = 0.09$
0.21	1.40(3)		1.46(5)	1.61(4)	1.68(2)
0.23	1.41(4)		1.48(6)	1.61(5)	
0.25	1.40(5)	1.44(4)	1.64(7)	1.60(9)	
0.26			1.66(10)	1.63(5)	
0.27	1.48(8)	1.64(10)	1.51(13)	1.76(13)	1.80(8)
0.28	1.50(12)		1.51(12)	1.61(7)	
0.29			2.08(33)	1.93(9)	1.90(7)
0.30	1.78(26)	1.58(11)	2.04(34)	1.70(20)	1.68(11)
0.32	2.07(57)		1.70(27)	2.12(31)	2.23(18)

$E_a^{(0)}$					
g_0	12^4		$8^3 \times 16$		
	$m_0 = 0.01$	$m_0 = 0.02$	$m_0 = 0.02$	$m_0 = 0.04$	$m_0 = 0.09$
0.21	1.36(1)		1.43(2)	1.48(1)	1.57(1)
0.23	1.34(1)		1.42(2)	1.50(2)	
0.25	1.32(2)	1.36(1)	1.53(2)	1.50(3)	
0.26			1.49(3)	1.49(2)	
0.27	1.38(3)	1.46(4)	1.46(4)	1.61(5)	1.71(3)
0.28	1.40(4)		1.46(4)	1.54(3)	
0.29			1.75(11)	1.65(3)	1.75(3)
0.30	1.51(8)	1.48(4)	1.66(10)	1.61(8)	1.70(4)
0.32	1.79(22)		1.49(8)	1.79(10)	1.88(6)

Table 12: Monte Carlo results for the energies of the ground state of the ρ' particle $E_{\rho'}^{(0)}$, its first excited state $E_{\rho'}^{(1)}$ and the ground state energy of the a particle $E_a^{(0)}$.

$E_{\omega}^{(0)}$					
g_0	12^4		$8^3 \times 16$		
	$m_0 = 0.01$	$m_0 = 0.02$	$m_0 = 0.02$	$m_0 = 0.04$	$m_0 = 0.09$
0.21	0.22(4)		0.27(1)	0.43(1)	0.71(1)
0.23	0.30(4)		0.37(2)	0.53(1)	0.80(2)
0.25	0.46(5)	0.47(4)	0.50(4)	0.64(3)	0.94(4)
0.26			0.62(4)	0.71(4)	1.00(6)
0.27	0.56(13)	0.40(15)	0.82(8)	0.78(5)	1.11(5)
0.28	0.54(12)		0.58(9)	0.80(8)	1.01(14)
0.29			0.80(12)	1.04(7)	1.32(8)
0.30	0.99(10)	1.03(4)	1.29(9)	0.91(21)	1.29(15)
0.32	1.22(11)		0.97(20)	0.97(15)	1.18(25)

$E_{\omega}^{(1)}$					
g_0	12^4		$8^3 \times 16$		
	$m_0 = 0.01$	$m_0 = 0.02$	$m_0 = 0.02$	$m_0 = 0.04$	$m_0 = 0.09$
0.21	1.68(3)		1.75(4)	1.76(3)	1.78(2)
0.23	1.74(6)		1.68(7)	1.75(5)	1.81(3)
0.25	1.97(18)	1.72(6)	1.79(18)	1.78(6)	1.90(6)
0.26			1.86(14)	1.86(11)	1.90(7)
0.27	1.82(34)	1.57(10)	2.23(51)	1.85(11)	2.05(11)
0.28	1.68(21)		1.64(10)	1.80(9)	1.88(9)
0.29			1.80(22)	2.22(27)	2.28(27)
0.30				1.74(12)	2.12(25)
0.32				2.13(31)	1.98(15)

$E_{b'}^{(0)}$					
g_0	12^4		$8^3 \times 16$		
	$m_0 = 0.01$	$m_0 = 0.02$	$m_0 = 0.02$	$m_0 = 0.04$	$m_0 = 0.09$
0.21	1.55(4)		1.67(7)	1.75(5)	1.71(3)
0.23	1.67(7)		1.42(18)	1.64(13)	1.67(8)
0.25	1.90(18)	1.64(7)	1.83(48)	1.70(8)	1.79(11)
0.26			1.57(23)	1.98(30)	1.91(16)
0.27	1.69(34)	1.56(14)	2.15(46)	1.82(13)	1.93(10)
0.28	1.49(21)		1.27(26)	1.68(23)	1.70(16)
0.29			1.69(24)	2.15(22)	2.15(19)
0.30				1.61(14)	2.04(17)
0.32				2.33(46)	2.02(19)

Table 13: Monte Carlo results for the energies of ground state of the ω particle $E_{\omega}^{(0)}$, its first excited state $E_{\omega}^{(1)}$ and the ground state of the b' particle $E_{b'}^{(0)}$.

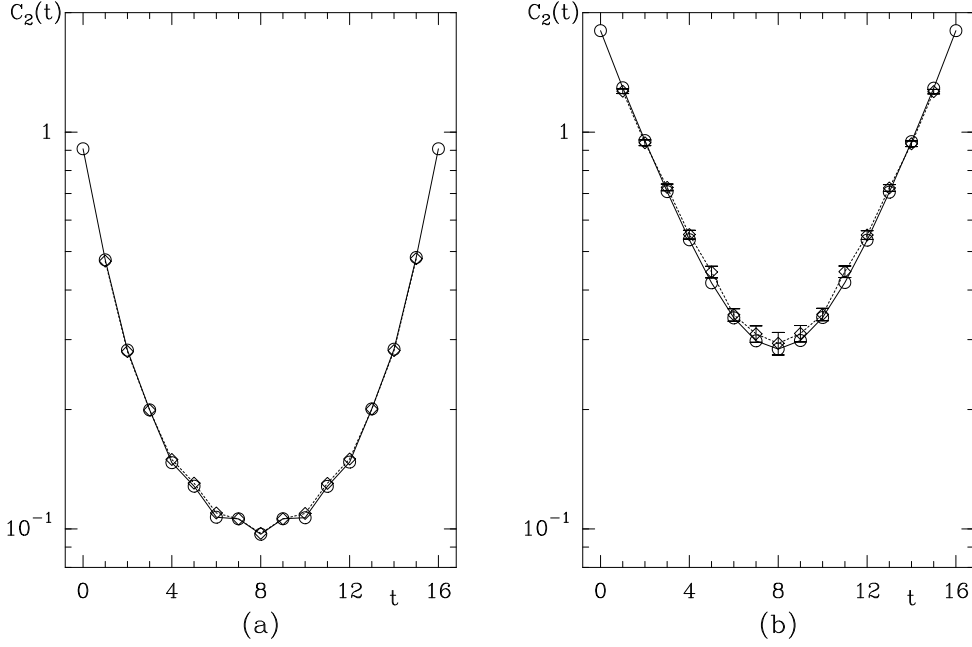


Figure 12: Influence of the annihilation part on the π propagator in the Monte Carlo calculation. Parameters and symbols are the same as in fig. 11 except that the diamonds now represent the complete propagator, eq. (4.6).

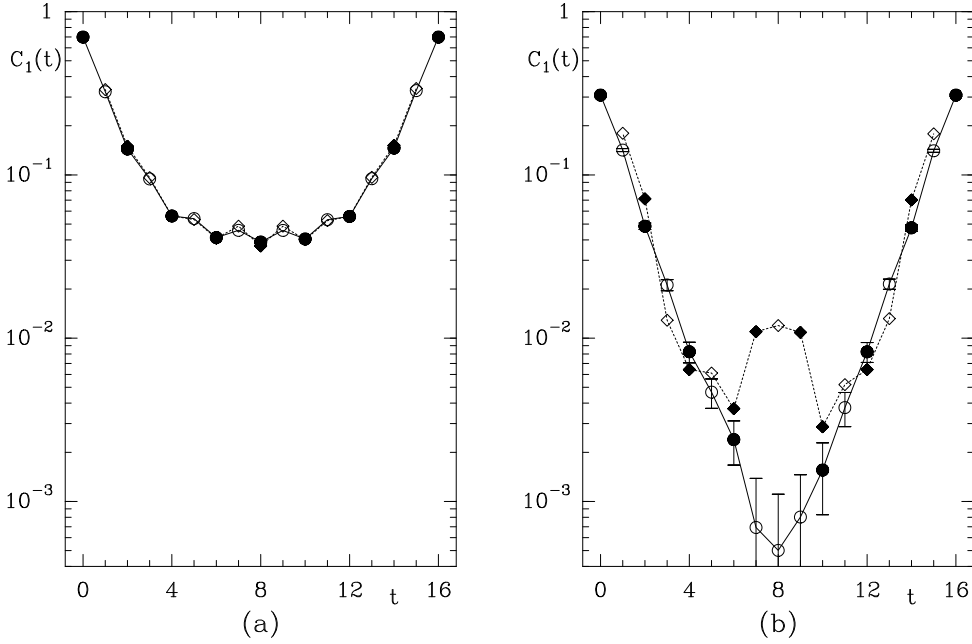


Figure 13: Influence of the annihilation part on the π'/σ propagator in the Monte Carlo calculation. Parameters and symbols are the same as in fig. 11 except that the diamonds now represent the complete propagator, eq. (4.6). See text for comments on (b).

For certain values of g_0 and m_0 we have also measured the annihilation part of the π and σ correlation functions, where 16 sets of gaussian random numbers were used in the stochastic estimator. As fig. 12 shows the influence in the π correlation function is small. Since the σ has the quantum numbers of the vacuum we have to subtract a constant from the σ correlation function before comparing it with the result without the annihilation part. As the constant is rather large (it is of $O(L_s^3 \langle \bar{\chi}\chi \rangle^2)$) in the middle of the correlation function in the broken phase we only see noise. A typical result is given in fig. 13. Within the errors the energies are unchanged and thus we can use the numbers in table 10 with some confidence. The discussion of our results will be postponed until section 5.

4.2 Schwinger-Dyson Equations

The fact that the Schwinger-Dyson equations have given such good results for the fermion propagator and chiral condensate encourages us to try a similar approach to meson propagators. In fig. 14 we show the Schwinger-Dyson equations for the fermion-antifermion composite propagator.

To get a manageable set of equations we have replaced the full kernel with the bare 4-fermi interaction. This gives us equations which are at the same level of accuracy as the order g_0 Schwinger-Dyson equations for the fermion propagator which, as we have already seen, yield a good approximation to the Monte Carlo results.

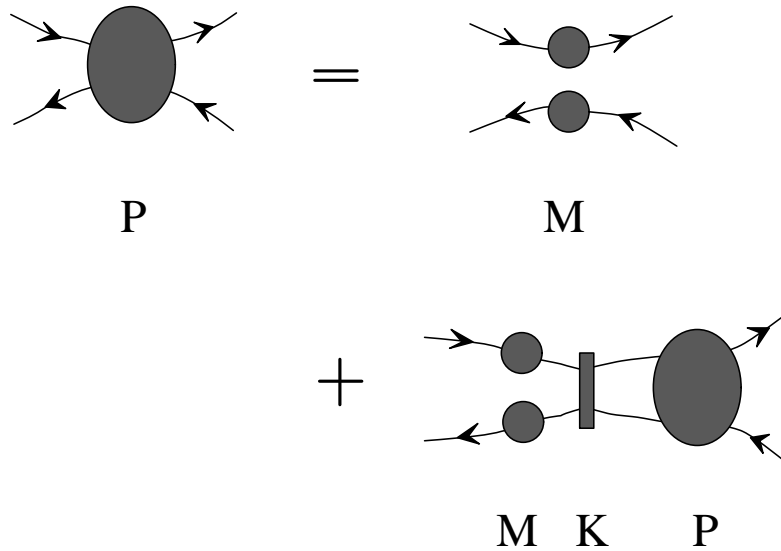


Figure 14: Pictorial representation of the Schwinger-Dyson equation for the meson propagators.

For the fermion line connected part of the local correlation functions we derive the following results in appendix A. Defining

$$C_i^{(0)}(t) = \frac{1}{L_t} \sum_{\omega} e^{i\omega t} \tilde{C}_i^{(0)}(\omega), \quad (4.13)$$

we find that the Fourier transforms $\tilde{C}_i^{(0)}(\omega)$ are given by

$$\begin{aligned} \tilde{C}_1^{(0)}(\omega) &= \frac{a_1(\omega)}{1 + a_1(\omega)2g_0(+3 - \cos \omega)}, \\ \tilde{C}_2^{(0)}(\omega) &= \frac{a_2(\omega)}{1 + a_2(\omega)2g_0(-3 - \cos \omega)}, \\ \tilde{C}_3^{(0)}(\omega) &= \frac{a_3(\omega)}{1 + a_3(\omega)2g_0(+1 - \cos \omega)}, \\ \tilde{C}_4^{(0)}(\omega) &= \frac{a_4(\omega)}{1 + a_4(\omega)2g_0(-1 - \cos \omega)}, \end{aligned} \quad (4.14)$$

where

$$a_i(\omega) = \frac{1}{V} \sum_k \frac{B_i^2 + F_t^2 \sin k_4 \sin(k_4 - \omega)}{[A^2 + F_t^2 \sin^2 k_4] [A^2 + F_t^2 \sin^2(k_4 - \omega)]}, \quad (4.15)$$

with

$$\begin{aligned} A^2 &\equiv N^2 + F_s^2 s^2, \\ B_1^2 &\equiv N^2 - F_s^2 s^2, \\ B_2^2 &\equiv N^2 + F_s^2 s^2, \\ B_3^2 &\equiv N^2 - \frac{1}{3} F_s^2 s^2, \\ B_4^2 &\equiv N^2 + \frac{1}{3} F_s^2 s^2, \end{aligned} \quad (4.16)$$

and

$$s^2 \equiv \sum_{i=1}^3 \sin^2 k_i. \quad (4.17)$$

The N , $F_s = F_1 = F_2 = F_3$ and $F_t = F_4$ have been defined in (2.14). The formulae for the fermion line disconnected part are also given in appendix A.

The principal interest in the fermion-antifermion channels lies in the energy spectrum, i. e., the eigenvalues of the transfer matrix. These energies can best be found on a long lattice which is why we used $8^3 \times 16$ lattices for most of our simulations. In the Schwinger-Dyson approach we can easily extend L_t to infinity, which allows a clean extraction of the full spectrum.

When $L_t = \infty$ the k_4 sum becomes an integral, which can be evaluated by contour integration. The general ‘‘bubble’’ a_i in (4.15) has the form

$$a_i(\omega) = \frac{1}{L_s^3} \sum_{\vec{k}} \mathcal{I}(A, B, \omega), \quad (4.18)$$

$$\mathcal{I}(A, B, \omega) = \int_0^{2\pi} \frac{dk_4}{2\pi} \frac{B^2 + F_t^2 \sin k_4 \sin(k_4 - \omega)}{[A^2 + F_t^2 \sin^2 k_4] [A^2 + F_t^2 \sin^2(k_4 - \omega)]}, \quad (4.19)$$

where A and B are functions of \vec{k} only. Evaluating this integral leads to the result

$$\mathcal{I}(A, B, \omega) = \frac{1}{A\sqrt{A^2 + F_t^2}} \left(\frac{A^2 + B^2}{2A^2 + F_t^2 - F_t^2 \cos \omega} - \frac{A^2 - B^2}{2A^2 + F_t^2 + F_t^2 \cos \omega} \right). \quad (4.20)$$

From the form of \mathcal{I} it is easy to see that the Fourier transform of the composite propagator is the ratio of two real polynomials in $\cos \omega$. Therefore the only singularities that can occur when L_s is finite are poles. A pole in the momentum-space propagator at $\omega = iE$ corresponds to a term $\propto \exp(-Et)$ in the real-space propagator, and a pole at $\omega = \pi + iE$ to a term $\propto (-1)^t \exp(-Et)$, so we can find the complete energy spectrum by locating all the poles in the momentum-space propagator. The order of these polynomials is proportional to the number of distinct terms in the sum over spatial momenta, so the number of energy levels should grow as L_s^3 .

Cursory inspection of the meson levels in tables 8–13 shows that many of the energy levels lie close to or above $2\mu_R$. In order to really understand what is happening above the fermion-antifermion threshold we need to take the infinite volume limit and see what happens as the excited states form a true continuum. We have already taken the $L_t \rightarrow \infty$ limit in eq. (4.20). We now let $L_s \rightarrow \infty$. The sum over \vec{k} in eq. (4.15) then turns into an integral, the analytic structure of which is worked out in appendix B. As L_s increases the poles above the threshold become denser and in the infinite volume limit become a cut.

In fig. 15 we sketch the singularity structure of \tilde{C} in the ω -plane and also give the integration contour needed to evaluate $C(t)$. $\tilde{C}(\omega)$ has cuts running from $\cos \omega = 1 + 2 \sinh^2 \mu_R$ to $\cos \omega = 7 + 2 \sinh^2 \mu_R$ and from $\cos \omega = -1 - 2 \sinh^2 \mu_R$ to $\cos \omega = -7 - 2 \sinh^2 \mu_R$. These cuts represent the continuum of fermion-antifermion states running from $E = 2\mu_R$ to $E = \cosh^{-1}(7 + 2 \sinh^2 \mu_R)$, the highest energy available to two fermions. The singularities in the phase-space function $\phi(r)$ (see appendix B) at $r = \pm 1$ lead to additional branch points within the cuts at $\cos \omega = \pm(3 + 2 \sinh^2 \mu_R)$ and $\cos \omega = \pm(5 + 2 \sinh^2 \mu_R)$.

The discontinuity across the cuts of \tilde{C} gives the spectral function ρ [28]. As well as these cuts \tilde{C} can also exhibit poles, which correspond to genuine bound states (stable mesons).

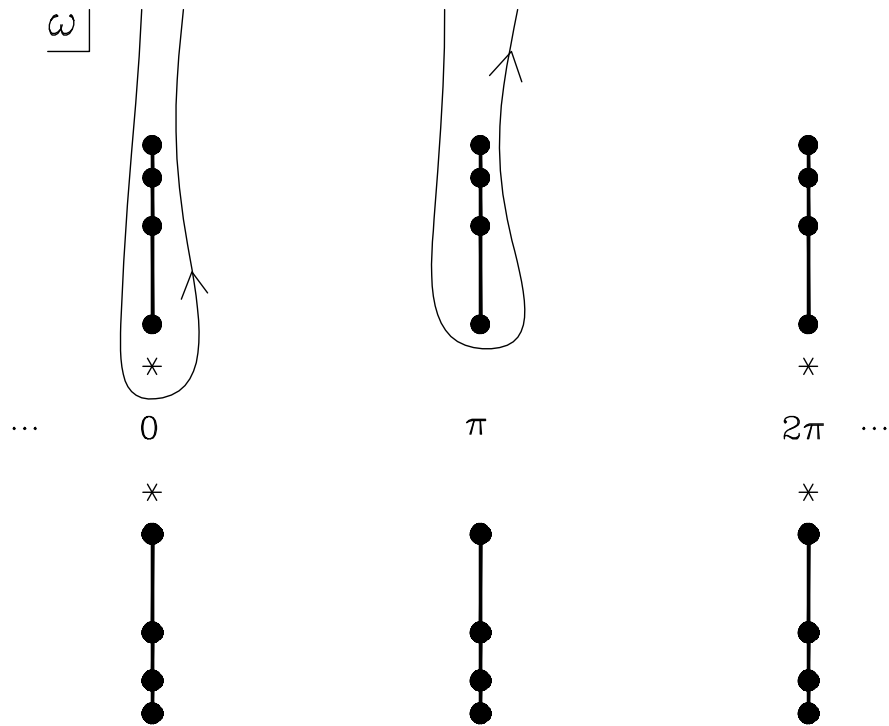


Figure 15: Singularity structure of $\tilde{C}_i^{(0)}(\omega)$ in the ω -plane. The solid lines are cuts, a $*$ is a pole and a \bullet is a branch point.

4.3 Finite Size Effects

We shall now study finite size effects for bound state masses using methods similar to those used in section 3.3 for the chiral condensate and the fermion mass. To do this we will consider finite size corrections to the “bubble” sums given in eq. (A.7). The main characteristic of these bubbles is that they involve two propagators with denominators U^+ and U^- . We take a slightly more general case where the physical masses (m_+ and m_-) in the two propagators can be different.

To find the change in the meson propagator we must investigate the effect of replacing the sum over loop momenta by an integral. Since we are interested in the meson mass we need to consider the case where the meson is on-shell, i. e., the 4-momentum $p = (0, 0, 0, iM)$ where M is the meson

mass. We now use the same Fourier transform argument as in section 3.3 to change a sum in momentum space to a sum in coordinate space.

A typical loop integral in eq. (A.7) has the form

$$\int \frac{d^4k}{(2\pi)^4} \frac{n(p, k)}{((p+k)^2 + m_+^2)(k^2 + m_-^2)}. \quad (4.21)$$

(The exact form of the numerator $n(p, k)$ is unimportant for asymptotic behaviour.) As before we need the large L_s limit of

$$\int \frac{d^4k}{(2\pi)^4} \exp(ik_1 L_s) \frac{n(p, k)}{((p+k)^2 + m_+^2)(k^2 + m_-^2)}. \quad (4.22)$$

Integrating exactly over k_1 and then with the saddle point approximation over the other three components of k gives a result

$$\propto \frac{1}{L_s} \exp(-\xi L_s) \equiv \Delta, \quad (4.23)$$

where

$$\xi = \frac{\sqrt{-M^4 + 2M^2 m_+^2 + 2M^2 m_-^2 + 2m_+^2 m_-^2 - m_+^4 - m_-^4}}{2M}. \quad (4.24)$$

The finite-size shift in the meson mass ought to be proportional to Δ .

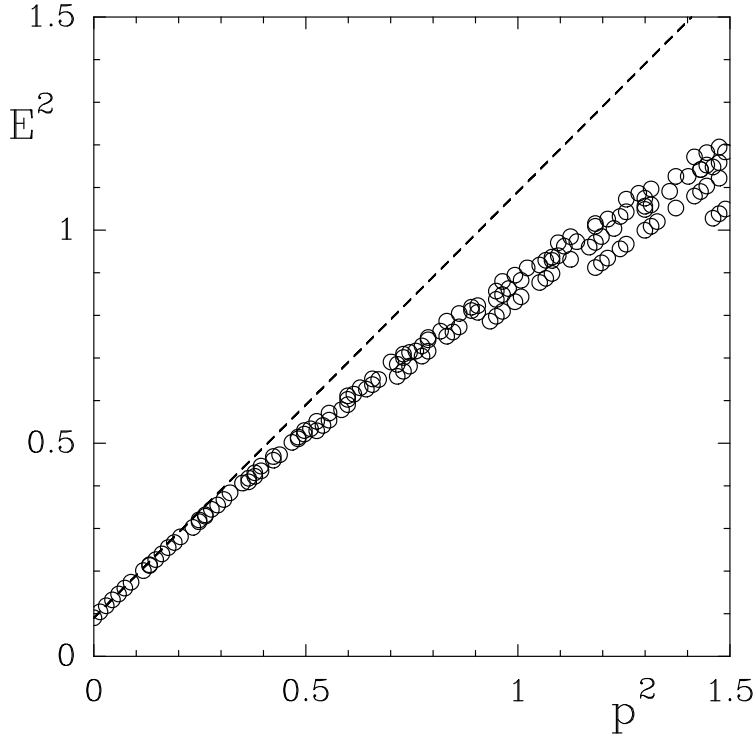


Figure 16: Dispersion relation of the π bound state obtained from Schwinger-Dyson calculations. Results are from a $52^3 \times \infty$ lattice with $m_0 = 0.01$ and $g_0 = 0.2476$, leading to $\mu_R = 0.20$ and $m_\pi = 0.301$.

We can consider various special cases of eq. (4.24). In the non-relativistic limit where the binding energy $B \equiv m_+ + m_- - M$ is small compared with M

$$\xi \rightarrow \sqrt{2m_{\text{reduced}}B} \equiv \sqrt{2 \left(\frac{m_+ m_-}{m_+ + m_-} \right) (m_+ + m_- - M)}, \quad (4.25)$$

recovering a result that can be found by solving the Schrödinger equation in a finite volume.

Other useful limits are the case $m_+ = m_-$ which gives $\xi = (4m_+^2 - M^2)^{1/2}/2$, which should apply to the pion when it is a true bound state, and $M = m_+ = m_-$ which gives $\xi = \frac{\sqrt{3}}{2}M$, relevant for finding the pion mass shift due to $\pi \rightarrow 2\pi \rightarrow \pi$ [24]. A further application of eq. (4.23) is to the process $f \rightarrow f + \pi \rightarrow f$, which will give a finite size shift to the fermion mass μ_R additional to that considered in section 3.3. This extra contribution will be of the form (4.23) with $\xi = \frac{m_\pi}{2\mu_R} \sqrt{4\mu_R^2 - m_\pi^2}$ and can become the leading term if the pion is light enough.

With the Schwinger-Dyson equations it is easy to study the restoration of Lorentz invariance. As an example in fig. 16 we look at the dispersion relation of the π bound state. We have plotted E^2 against \vec{p}^2 for all possible \vec{p} values which occur on a lattice with $L_s = 52$. When \vec{p}^2 can be realised in inequivalent ways we have plotted all the possible energies. We see that the Einstein relationship $E^2 = m^2 + \vec{p}^2$ holds well up to $\vec{p}^2 \approx 0.2$ and that spherical symmetry (E^2 independent of the momentum direction) holds up to $\vec{p}^2 \approx 0.5$.

Although Lorentz invariance is restored we observe at most partial flavour symmetry restoration: The correlation functions for the Goldstone π and the non-Goldstone π look rather different.

5 Meson Propagators and Spectroscopy

We now compare the correlation functions found by solving the order g_0 Schwinger-Dyson equations with those from Monte Carlo. We show some Monte Carlo propagators together with the Schwinger-Dyson correlation functions calculated with the same bare mass and the coupling chosen such that the renormalised fermion masses agree. In view of the fact that the order g_0 Schwinger-Dyson equations do not reproduce exactly the critical coupling found in the Monte Carlo calculations it is not surprising that a shift in the coupling is necessary to achieve agreement in the propagators. Indeed the shift is about the same as the difference between the critical couplings. Looking at figures 17–19 we find a good agreement between the Schwinger-Dyson and Monte Carlo data. The agreement is of course best at small g_0 but even at large g_0 is still satisfactory.

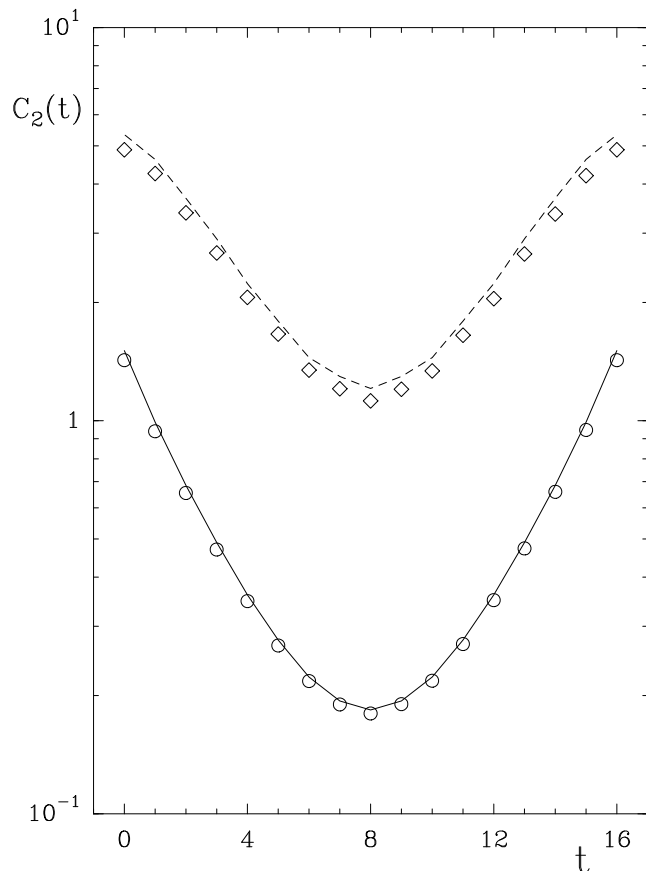


Figure 17: Comparison of Schwinger-Dyson and Monte Carlo data for the π propagators $C_2^{(0)}(t)$ (solid lines, circles) and $C_2^{(w)}(t)$ (dashed lines, diamonds). The results come from calculations on an $8^3 \times 16$ lattice at $m_0 = 0.02$ and $g_0 = 0.27$ (Monte Carlo). For the Schwinger-Dyson calculation we used $g_0 = 0.2491$ leading to the same fermion mass as the Monte Carlo calculation.

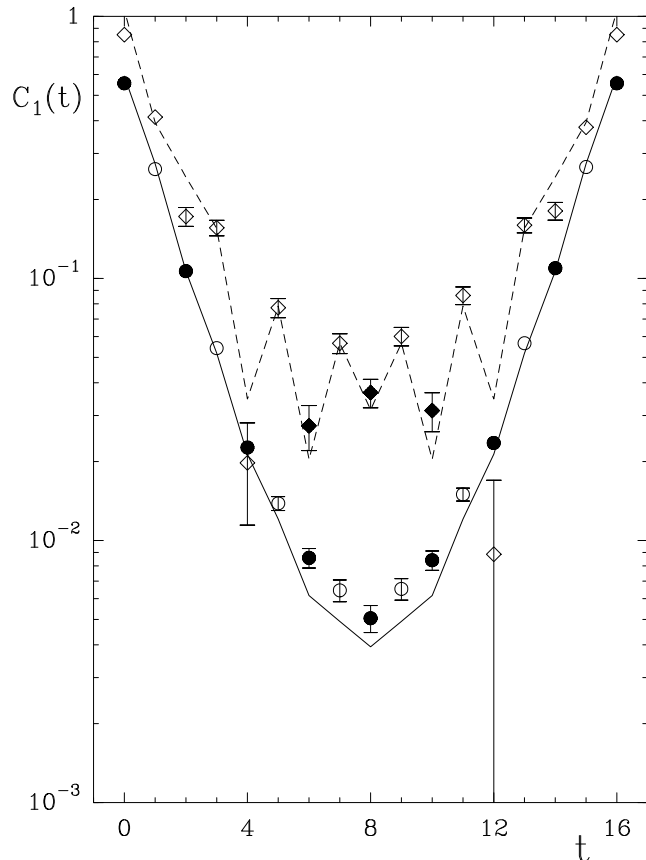


Figure 18: Comparison of Schwinger-Dyson and Monte Carlo data for the π'/σ propagators. Symbols and parameters are the same as in fig. 17. Solid symbols represent negative values.

Like the Monte Carlo measurements the Schwinger-Dyson equations give a rather small annihilation contribution to the correlation functions. The largest effect is seen for the σ particle deep in the broken phase. An example is shown in fig. 20. In distinction to the Monte Carlo approach there are no noise problems. Let us note that the order g_0 Schwinger-Dyson equations satisfy the Ward identity [25, 26]

$$\frac{d\langle\bar{\chi}\chi\rangle}{dm_0} = \sum_t (-1)^t C_1^{(0)}(t), \quad (5.1)$$

if one uses the full correlation functions (but not if the annihilation contribution is neglected).

From now on we just look at the fermion line connected part of the propagators. In figures 21–23 we compare energy levels from the Monte Carlo with those from the Schwinger-Dyson calculations. In these figures we

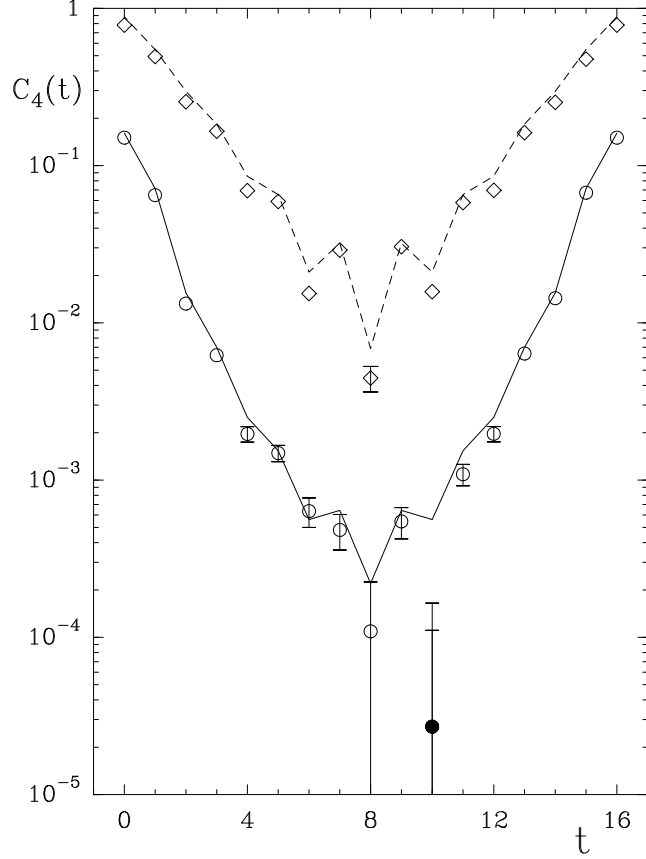


Figure 19: Comparison of Schwinger-Dyson and Monte Carlo data for the ρ/b propagators. Symbols and parameters are the same as in fig. 17. Solid symbols represent negative values.

plot some measured values from tables 8–11 against the renormalised fermion mass. The s -wave states are represented by solid lines (Schwinger-Dyson) and solid circles (Monte Carlo), the p -wave states by dashed lines (Schwinger-Dyson) and open circles (Monte Carlo). The dotted lines represent $2\mu_R$, so bound states lie below this line. The states that lie above the threshold would form the continuum on the infinite lattice possibly including resonances. One must be careful about states that lie slightly below the threshold because they might appear to be bound due to the finite volume.

Let us discuss the pictures in more detail. The π picture (fig. 21) shows that the first two levels are in very good agreement. It is thus reasonable to expect that the higher levels are correctly represented by the Schwinger-Dyson formalism. The large gap between the second and third level explains the success of the two level fit formula. Obviously we find a bound state with the quantum numbers of the π in the broken phase. This state is the pseudo-Goldstone boson associated with chiral symmetry breaking, and its

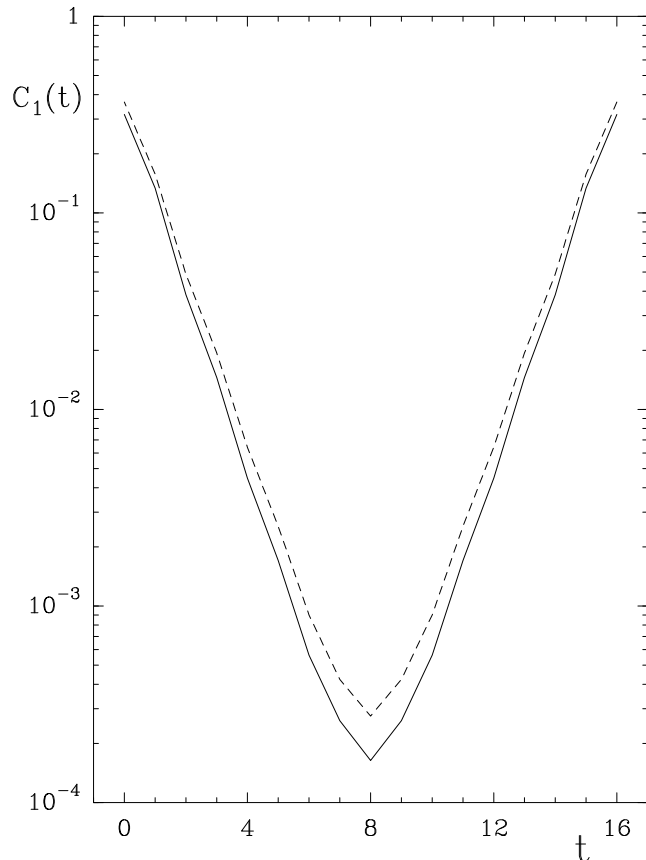


Figure 20: *Influence of the annihilation part on the π'/σ propagator in the Schwinger-Dyson calculation. The solid line is $C_1^{(0)}(t)$ calculated without the annihilation part, the dashed line represents the result including it. The parameters are the same as in fig. 13(b), except that $g_0 = 0.2975$ leading to the same fermion mass as the Monte Carlo data at $g_0 = 0.32$.*

mass tends to zero as m_0 tends to zero as one expects. The picture shows avoided level crossing suggesting the possible existence of a resonance [24] in the symmetric phase.

In the π'/σ picture (fig. 22) we see two states with opposite parity (the σ is the top curve). For small μ_R the ground state energies are reproduced by the Schwinger-Dyson equations. There is somewhat less good agreement for large values of μ_R . It is not clear whether we have a slightly bound state for the σ . The ground state energy of the π' is always close to $2\mu_R$.

Finally in fig. 23 we show levels in the ρ/b channel (the ρ is the solid curve). The agreement for the ρ ground state is good, for the excited states the fit cannot really resolve the levels lying relatively close to each other. The ground state of the ρ does not appear to be bound. The ρ'/a and ω/b' pictures look similar.

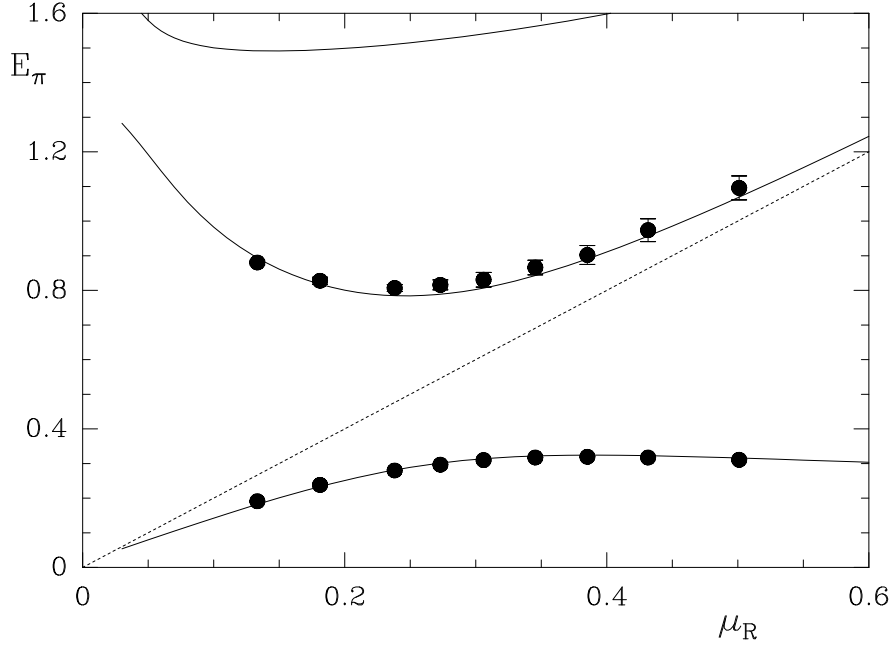


Figure 21: Energy levels in the π channel on $8^3 \times 16$ (Monte Carlo) and $8^3 \times \infty$ lattices (Schwinger-Dyson) at $m_0 = 0.02$. The dotted line represents the threshold $E_\pi = 2\mu_R$.

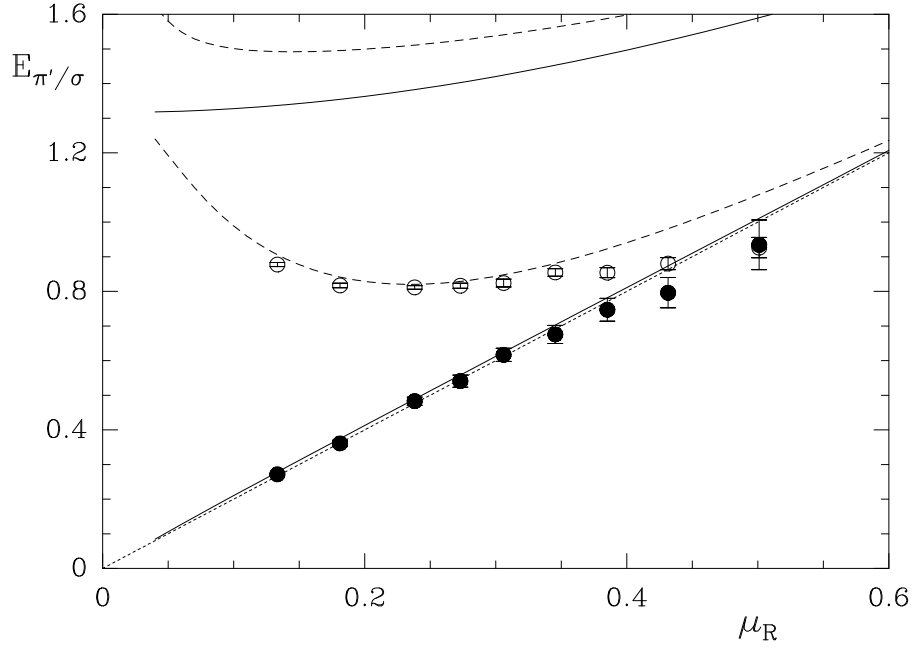


Figure 22: Energy levels in the π'/σ channel on $8^3 \times 16$ (Monte Carlo) and $8^3 \times \infty$ lattices (Schwinger-Dyson) at $m_0 = 0.02$. The dotted line represents the threshold $E_{\pi'/\sigma} = 2\mu_R$. The solid line and the black symbols represent $E_{\pi'}$ while the dashed lines and open symbols represent E_σ .

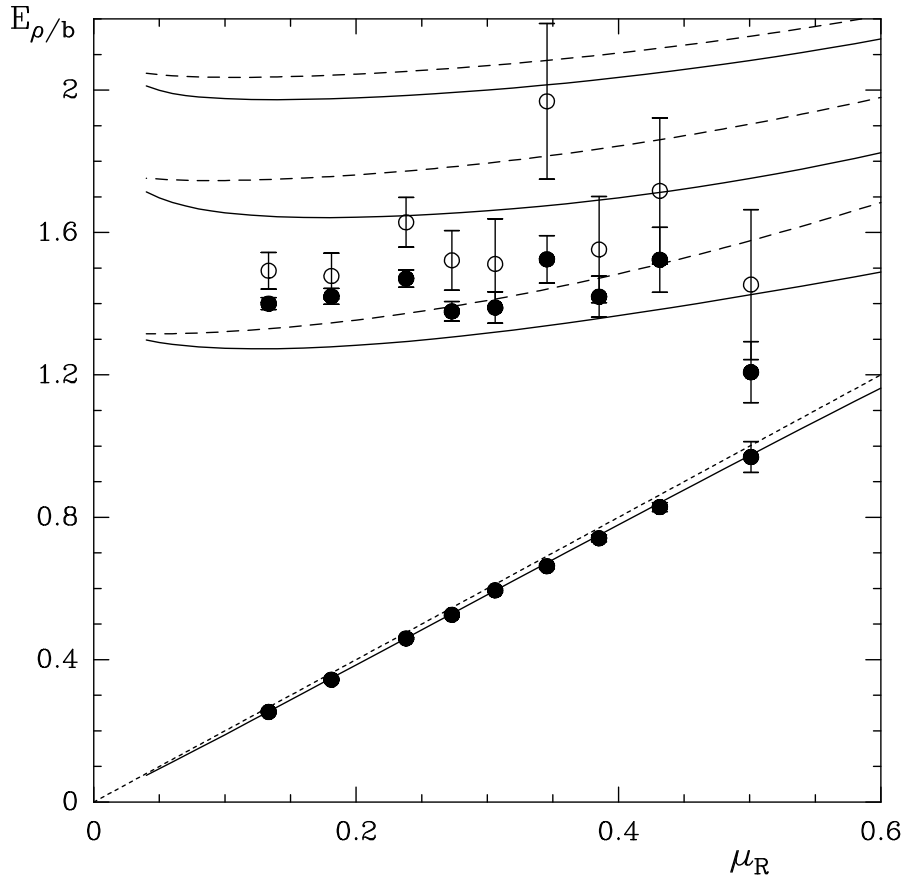


Figure 23: Energy levels in the ρ/b channel on $8^3 \times 16$ (Monte Carlo) and $8^3 \times \infty$ lattices (Schwinger-Dyson) at $m_0 = 0.02$. The dotted line represents the threshold $E_{\rho/b} = 2\mu_R$. The solid line and the black symbols represent E_ρ while the dashed lines and open symbols represent E_b .

We now look at what is happening in large volumes. In fig. 24 we have plotted the energy levels of the π on a $52^3 \times \infty$ lattice (solid lines). Also shown are the ground state energies for smaller lattices together with Monte Carlo data. For large μ_R we have a bound state which for small values of μ_R turns into a resonance, whose energy was calculated from the infinite volume spectral function (see below). In the finite volume the resonance reveals itself by avoided level crossing. Finite size effects for the ground state are largest close to the threshold.

For comparison we also display energy levels of the σ and ρ on a large lattice along with the resonance energies (figures 25 and 26). In both cases there are bound states for large μ_R . We would like to point out that the ρ resonance and bound state energies stay large even as $m_0 \rightarrow 0$ (see below).

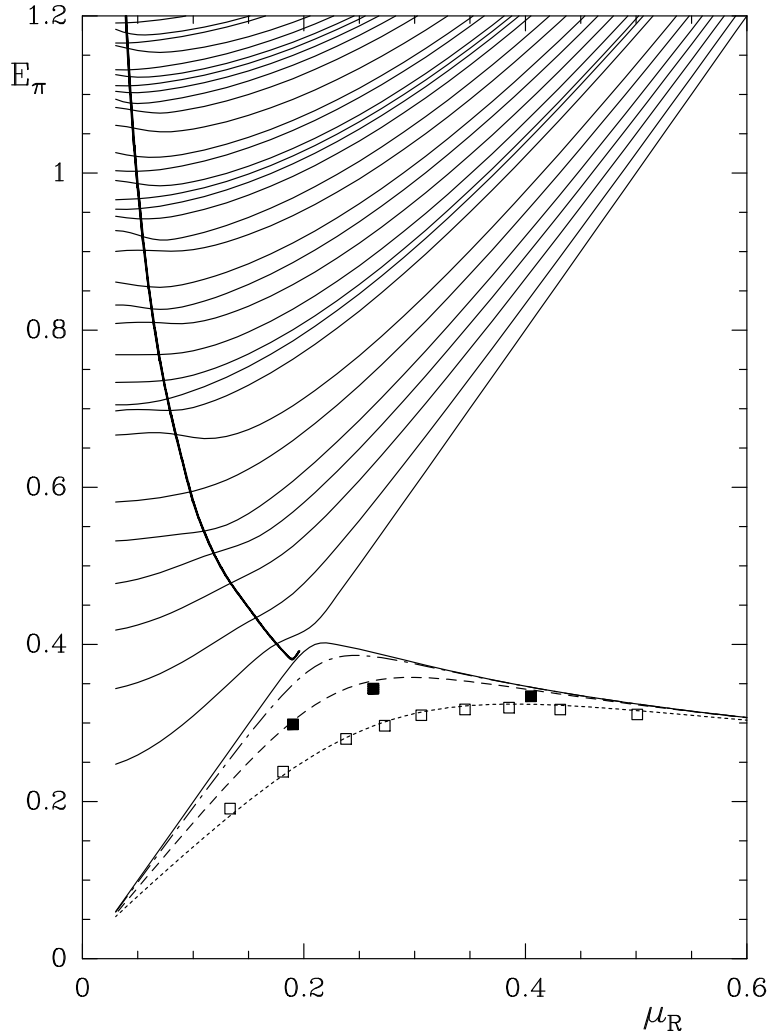


Figure 24: Energy levels of the π particle on a $52^3 \times \infty$ lattice ($m_0 = 0.02$). Also shown are the ground state energies on $20^3 \times \infty$, $12^3 \times \infty$ and $8^3 \times \infty$ lattices together with Monte Carlo results from 12^4 and $8^3 \times 16$ lattices. The solid line indicates the resonance energy at infinite volume.

As the volume increases the density of levels above threshold increases further until for infinite volume we have a continuum and can now define spectral functions $\rho_{\pm}^{(l)}$, $l \in \{0, 1, w\}$:

$$C^{(l)}(t) = \int_0^{\infty} \frac{dE}{\pi} e^{-E|t|} \rho_+^{(l)}(E) + (-1)^t \int_0^{\infty} \frac{dE}{\pi} e^{-E|t|} \rho_-^{(l)}(E). \quad (5.2)$$

They are calculated from the discontinuities across the cuts and poles of the amplitude \tilde{C} in fig. 15:

$$\begin{aligned} \rho_+^i &= \text{Im } \tilde{C}^i(iE + \epsilon), \\ \rho_-^i &= \text{Im } \tilde{C}^i(iE + \pi + \epsilon), \quad \epsilon \rightarrow +0. \end{aligned} \quad (5.3)$$

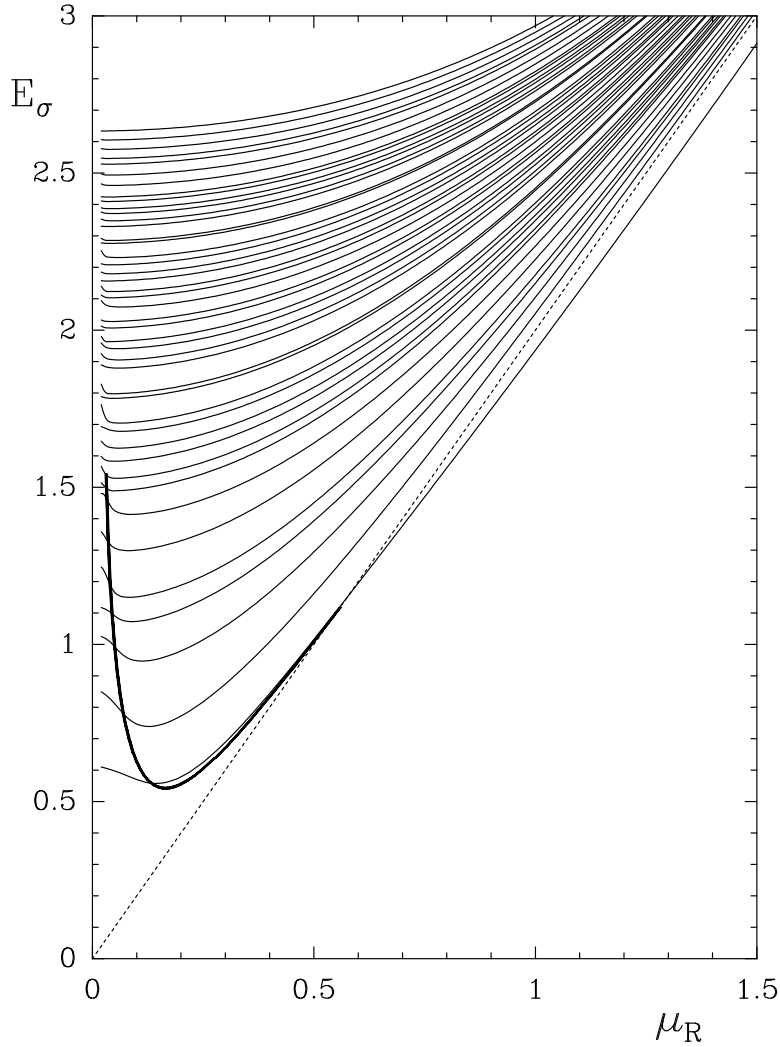


Figure 25: *Energy levels of the σ particle on a $20^3 \times \infty$ lattice ($m_0 = 0.02$). The solid line indicates the resonance energy at infinite volume. The dotted line is the threshold.*

Let us look at the π spectral function in more detail. In this case we need only one spectral function ρ_+ , because ρ_- is zero. Above $2\mu_R$ there is a continuum of states (fig. 27b). In the symmetric phase fig. 27a shows a resonance. We can tell that this ‘bump’ is really a resonance because we have analytically continued the amplitude to the second Riemann sheet and found a pole. Locating the pole gives us both the real and imaginary parts of the pion mass and so tells us the rate Γ_π at which the π resonance decays to a fermion-antifermion pair. In the broken phase the spectral function of the π contains a δ -function contribution. This shows that the resonance has turned into a bound state.

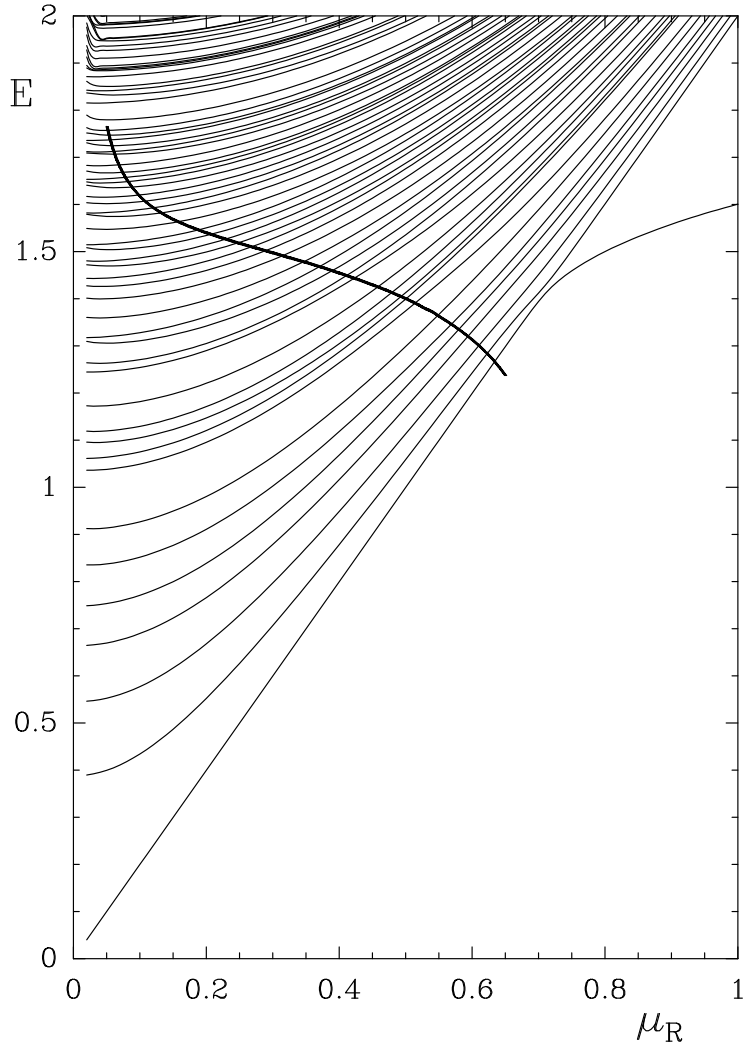


Figure 26: *Energy levels of the ρ particle on a $20^3 \times \infty$ lattice ($m_0 = 0.02$). The solid line indicates the resonance energy at infinite volume.*

In fig. 28 we show the π resonance mass m_π and width Γ_π in the symmetric phase. Note that the ratio Γ_π/m_π decreases towards zero as we approach the critical point, suggesting that the physical strength of the meson-fermion coupling decreases as we go to the continuum limit. This is what we would expect in a ‘trivial’ theory.

In fig. 29 we show the spectral function of the σ . There is a strong and narrow resonance just above the threshold. This corresponds to the scalar state at $2\mu_R$ that Nambu and Jona-Lasinio found [2].

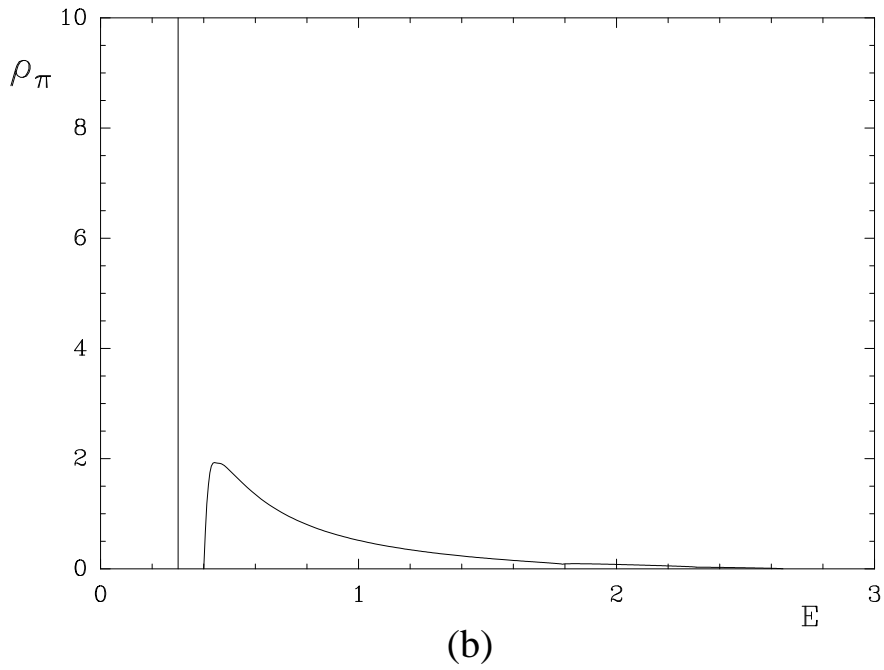
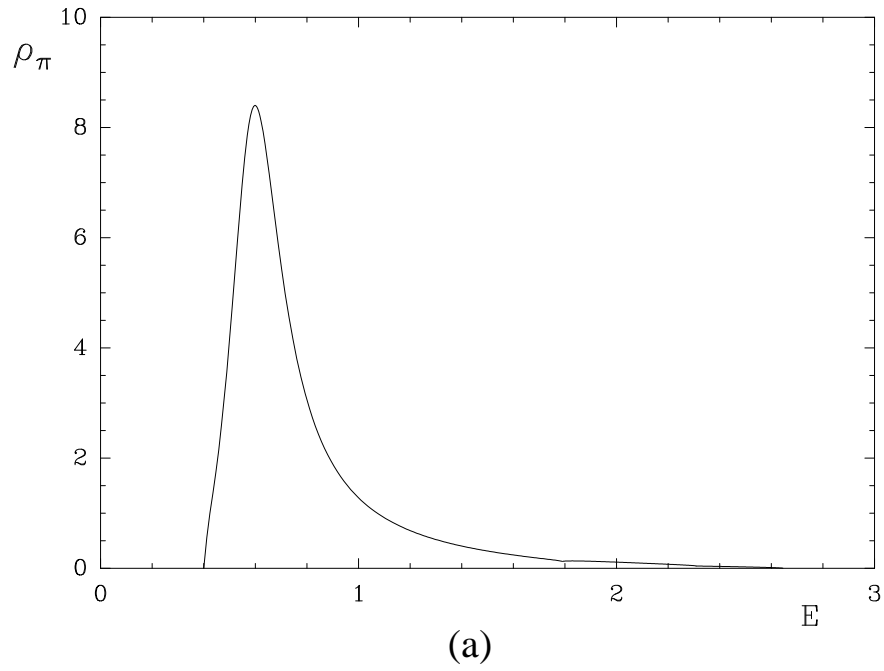


Figure 27: Spectral function of the π particle: (a) in the symmetric phase ($m_0 = 0.04$, $g_0 = 0.2056$ leading to $\mu_R = 0.20$), (b) near g_c ($m_0 = 0.01$, $g_0 = 0.2476$ leading to $\mu_R = 0.20$).

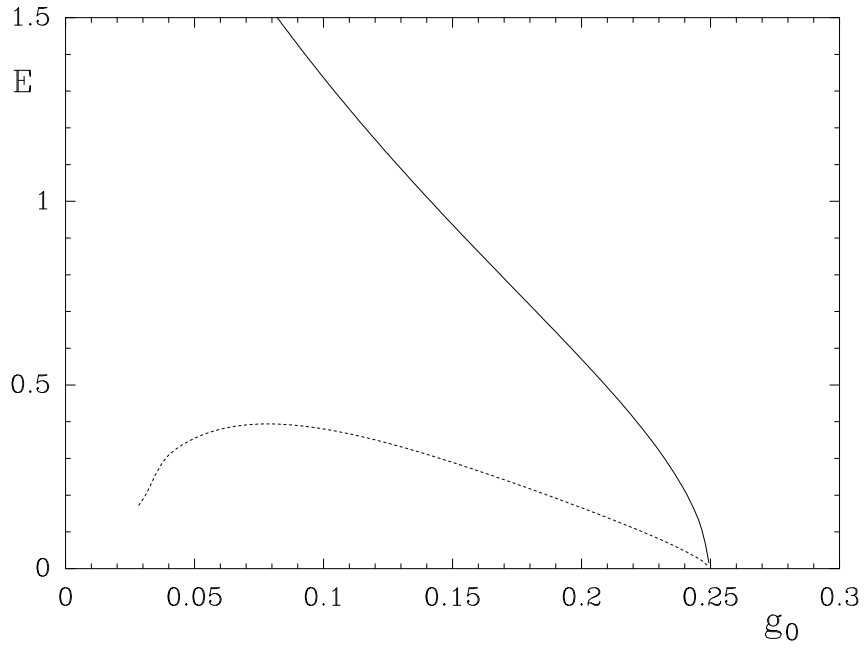


Figure 28: Resonance mass (solid line) and width (dotted line) of the π particle at $m_0 = 0$.

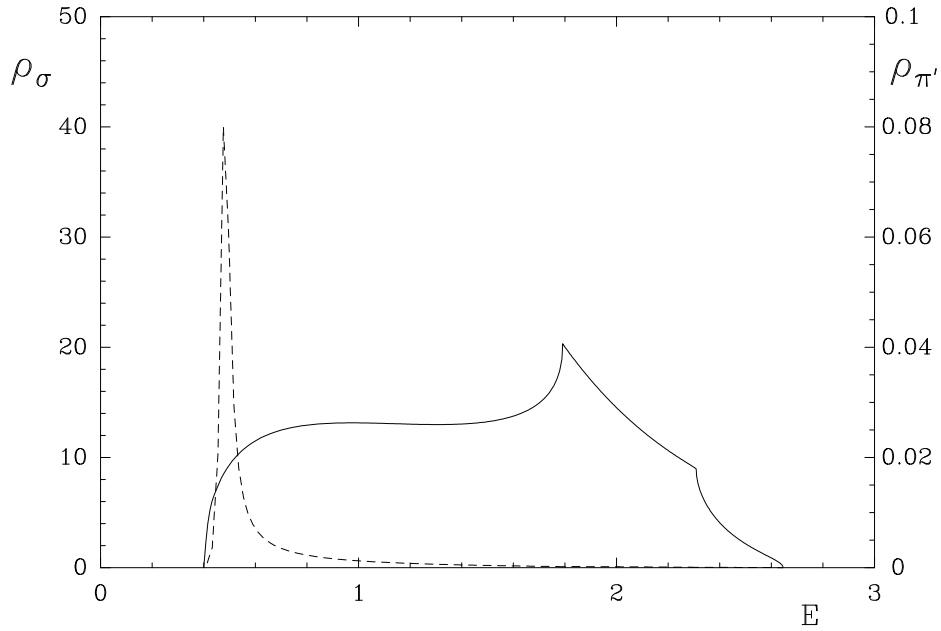


Figure 29: Spectral function of the σ (dashed line) and π' (solid line) particles near g_c ($m_0 = 0.01$, $g_0 = 0.2476$ leading to $\mu_R = 0.20$). (Note that the two functions have been shown at very different scales.)

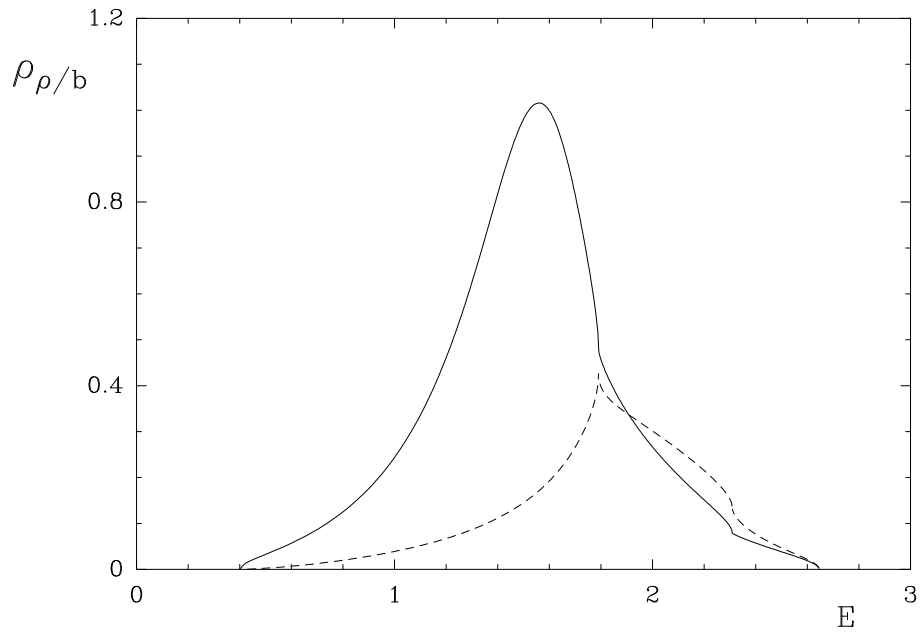


Figure 30: Spectral function of the ρ (solid line) and b (dashed line) particles in the symmetric phase ($m_0 = 0.04$, $g_0 = 0.2056$, leading to $\mu_R = 0.20$).

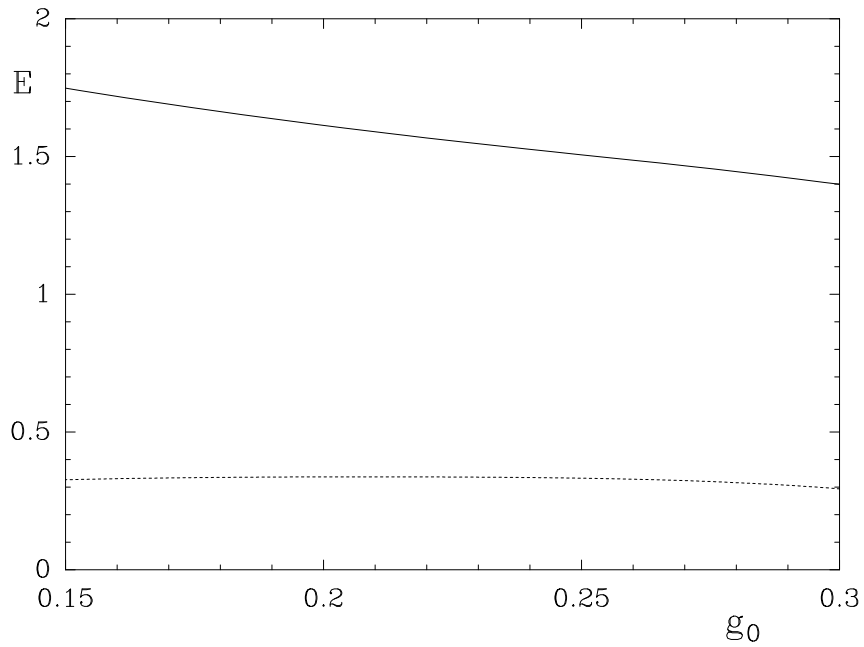


Figure 31: Resonance mass (solid line) and width (dotted line) of the ρ particle at $m_0 = 0.02$.

Next we look at the picture of the ρ and b spectral functions (fig. 30). We see that the ρ is a resonance. Although this would initially appear interesting we find that this resonance never becomes light compared with the inverse lattice spacing. Even at the critical point it has a mass of about 1.5 (see

fig. 31). In the b channel there is only a continuum. Note that the s - and p -wave show a different threshold behaviour ($\rho \propto [E - 2\mu_R]^{1/2}$ for the s -wave, $\rho \propto [E - 2\mu_R]^{3/2}$ for the p -wave).

As well as the resonance we see two other curious features, sharp discontinuities in the slope of the spectral function at energies of approximately 1.8 and 2.3. In general they appear at $E = \cosh^{-1}(3 + 2\sinh^2\mu_R)$ and $\cosh^{-1}(5 + 2\sinh^2\mu_R)$. These are examples of van Hove singularities [27]. Such singularities are familiar from solid state physics and result from saddle points in the fermions' energy momentum relation. At the corresponding energies the density of states is singular leading to singularities in the spectral functions (see appendix B). These singularities are also present (though often less noticeable) in the other channels. The van Hove singularities introduce a complication when analytically continuing onto the non-physical Riemann sheet (see fig. 15). Because there are branch points we reach different sheets depending on where we cross the axis in relation to these singularities. The sheet which is relevant for the continuum limit of the theory is the one reached by crossing the axis between the threshold and the first van Hove singularity. The other sheets only exist because of the saddle points in the lattice fermion dispersion relation at $\vec{k} = (\frac{\pi}{2}, 0, 0), (\frac{\pi}{2}, \frac{\pi}{2}, 0)$ etc., and so should have no relevance to the continuum. All the resonances we have seen are on this 'low energy' sheet.

The ρ'/a channel is similar to the ρ/b . We see similar resonances (one of each parity) which in the continuum limit go to the cutoff. For the ω/b' the Monte Carlo results indicate that these particles are also heavy.

6 Renormalisation Group Flow

In this section we study the renormalisation group flow in our model. We consider dimensionless ratios of physical quantities and attempt to find lines of constant physics, i. e., lines where all those ratios are constant, independent of the cutoff. Only in regions where such lines exist is the theory renormalisable [11, 29, 30]. Since we are interested in physical quantities we should only look at the ratios involving the particles whose correlation lengths diverge at the critical point, namely the fermion, π and σ . Other states (such as the ρ) with energies near $1/a$ are irrelevant in this context.

In fig. 32 we show $E_\pi^{(0)}/\mu_R$ and μ_R/f_π for the Monte Carlo results on an $8^3 \times 16$ lattice. There is no region where the lines are parallel to each other, thus there are no lines of constant physics. There are however two caveats to this picture. The first is that we have large finite size effects and secondly that in the symmetric phase the π is a resonance, and so $E_\pi^{(0)}$ no longer corresponds to the pion mass (see fig. 24). The upper right hand corner suffers least from these problems, and here the Monte Carlo results can be taken at face value. These difficulties can be circumvented by use of Schwinger-Dyson equations. In fig. 33 we show the Schwinger-Dyson results on $8^3 \times \infty$ and $20^3 \times \infty$ lattices. Comparison of the two volumes shows the features which are robust. In the broken phase the lines of constant mass ratio flow towards the critical point but curve away just before reaching it.

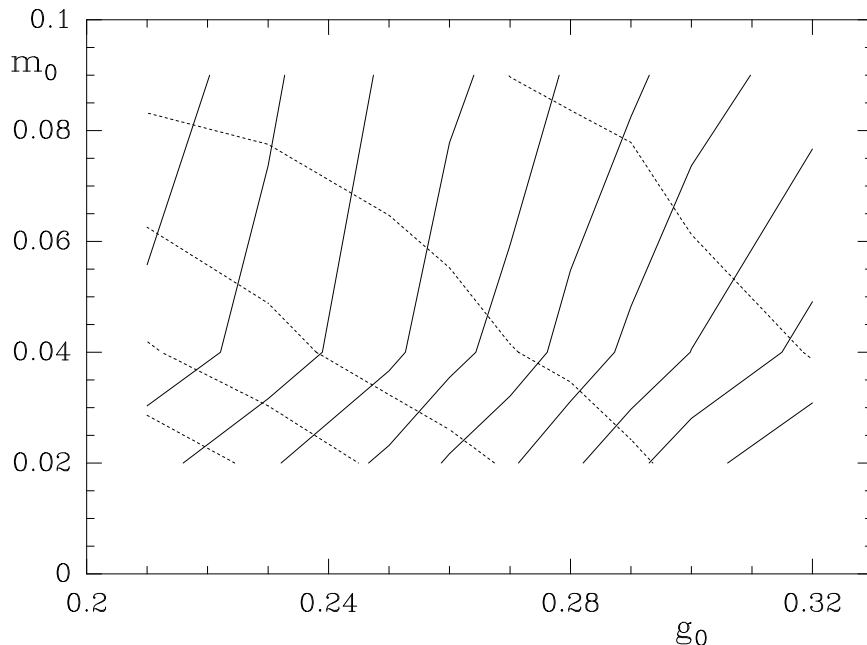


Figure 32: Lines of constant $E_\pi^{(0)}/\mu_R$ (solid) and of constant μ_R/f_π (dotted) in the plane of the bare parameters from Monte Carlo results on an $8^3 \times 16$ lattice. $E_\pi^{(0)}/\mu_R = 0.7$ to 1.6 in steps of 0.1 (right to left). $\mu_R/f_\pi = 1.5$ to 3.5 in steps of 0.5 (left to right).

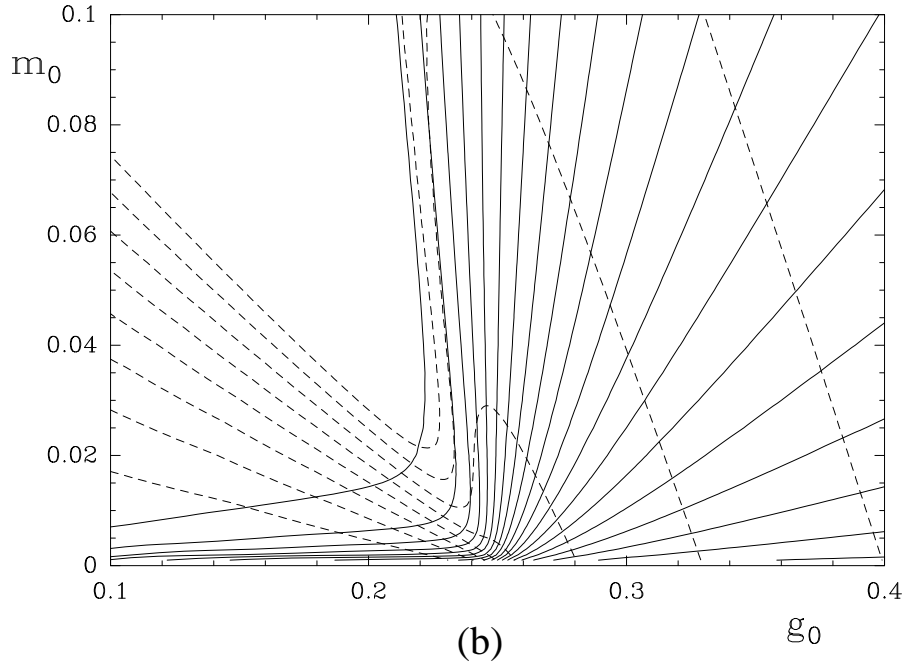
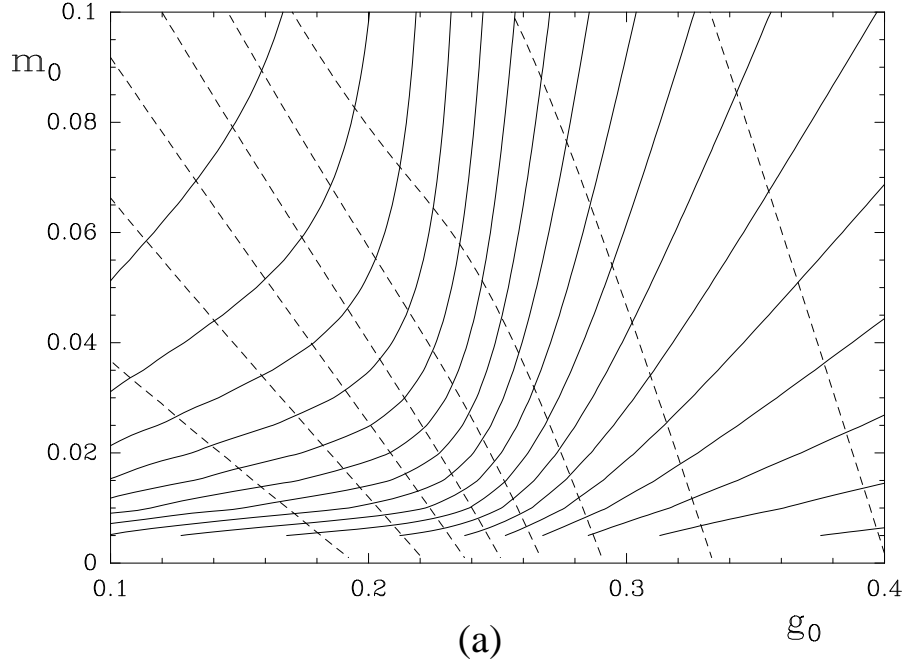


Figure 33: Lines of constant $E_\pi^{(0)}/\mu_R$ (solid) and of constant μ_R/f_π (dashed) from Schwinger-Dyson calculations on $8^3 \times \infty$ (a) and $20^3 \times \infty$ (b) lattices. For $E_\pi^{(0)}/\mu_R$ the ratios are: (a) 0.2 to 1.8 and (b) 0.1 to 1.9 in steps of 0.1. In both figures $\mu_R/f_\pi = 0.5$ to 4.0 in steps of 0.5.

In the symmetric phase the ratio is always just below 2 because we have used $E_\pi^{(0)}$, the lowest energy level in the π channel. (When comparing these figures with fig. 32 remember that the equivalence between the Monte Carlo and the Schwinger-Dyson equations is not exact, there being a small shift in g_c between them.)

Extrapolating to infinite volume by the Schwinger-Dyson equations gives fig. 34. In this limit we can identify resonances and find their masses. These are shown in the diagram as dotted lines. Now all the lines flow into the critical point. This type of flow diagram was also found in QED [11]. In the broken phase we can see that the lines of constant mass ratio, fig. 34, and the lines of constant μ_R/f_π , fig. 35, take different paths just as in fig. 32, again showing that there are no lines of constant physics.

To test for the existence of lines of constant physics in the symmetric phase we have looked at the ratio between m_π and Γ_π . These quantities are found from the real and imaginary parts of the pole position. In fig. 36 lines of constant Γ_π/m_π are compared with curves of constant μ_R/m_π . Once again the different flows cross. In this phase too there are no lines of constant physics. To display this information another way we show in fig. 37 the way in which Γ_π/m_π varies along a particular curve of constant mass ratio ($\mu_R/m_\pi = 0.20$). Because the phase space available for the decay depends on the mass ratio the variation in Γ_π/m_π along this path is not due to kinematics, but must reflect a variation in the strength of the coupling between the π

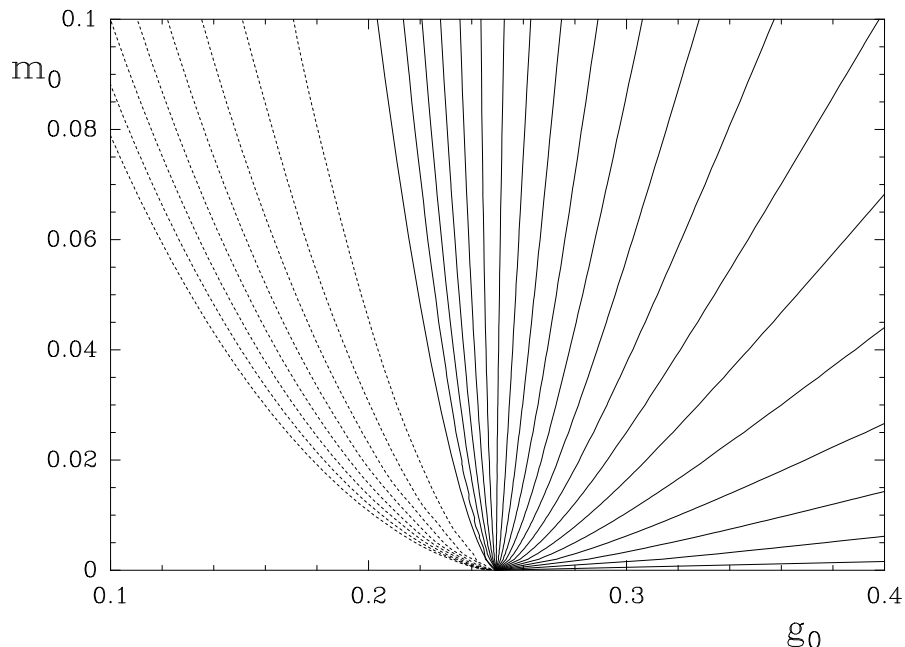


Figure 34: Lines of constant m_π/μ_R on an ∞^4 lattice. Solid lines are used where the π is a bound state and dotted lines where it is a resonance. The ratios are 0.1 to 2.0 in steps of 0.1 (bound state) and 3 to 10 in steps of 1 (resonance).

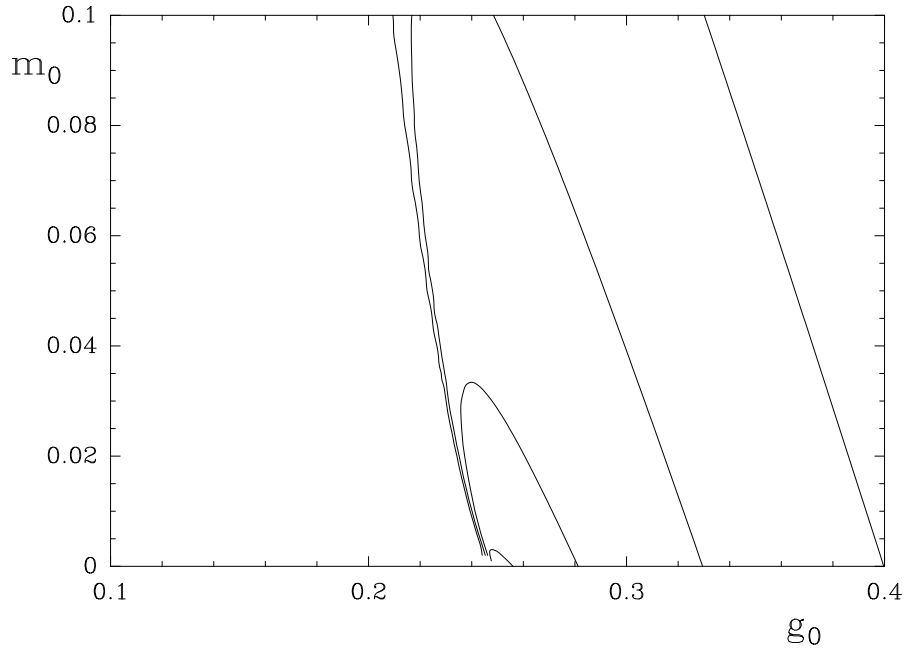


Figure 35: Lines of constant μ_R/f_π on an ∞^4 lattice. The ratio runs from 2.5 (inner curve) to 4.0 (outer curve) in steps of 0.5.

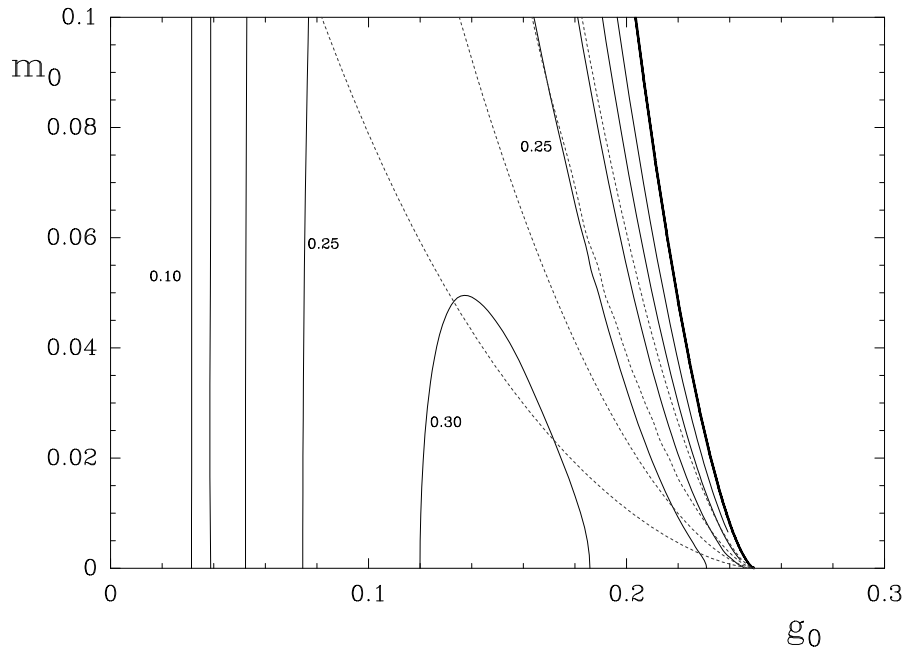


Figure 36: A comparison between the flows of constant Γ_π/m_π (solid lines) and constant μ_R/m_π (dotted lines) in the region where the π is a resonance. μ_R/m_π runs from 0.1 to 0.4 in steps of 0.1, Γ_π/m_π from 0.1 to 0.3 in steps of 0.05.

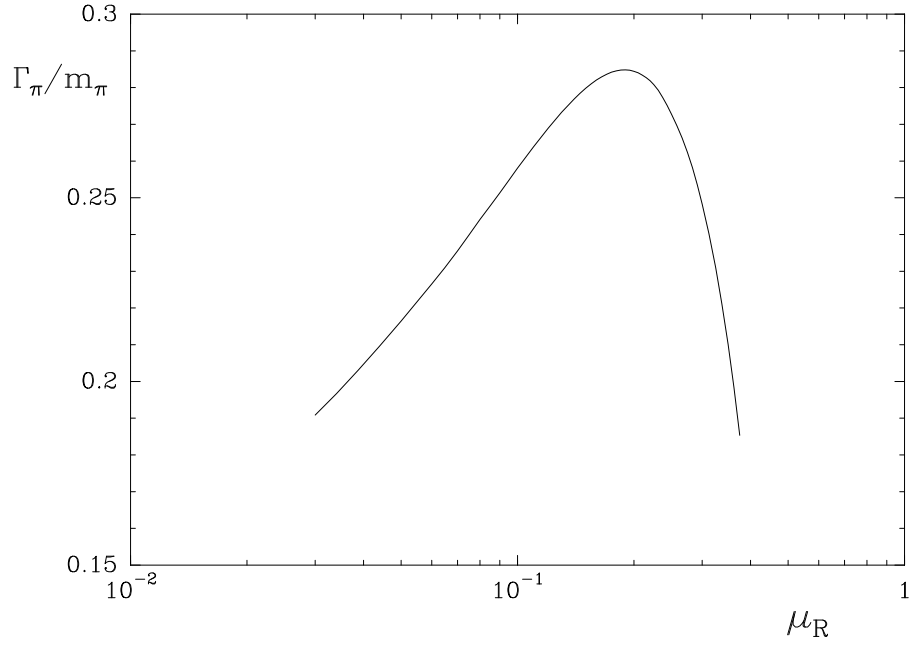


Figure 37: The variation in Γ_π/m_π along the curve $\mu_R/m_\pi = 0.20$.

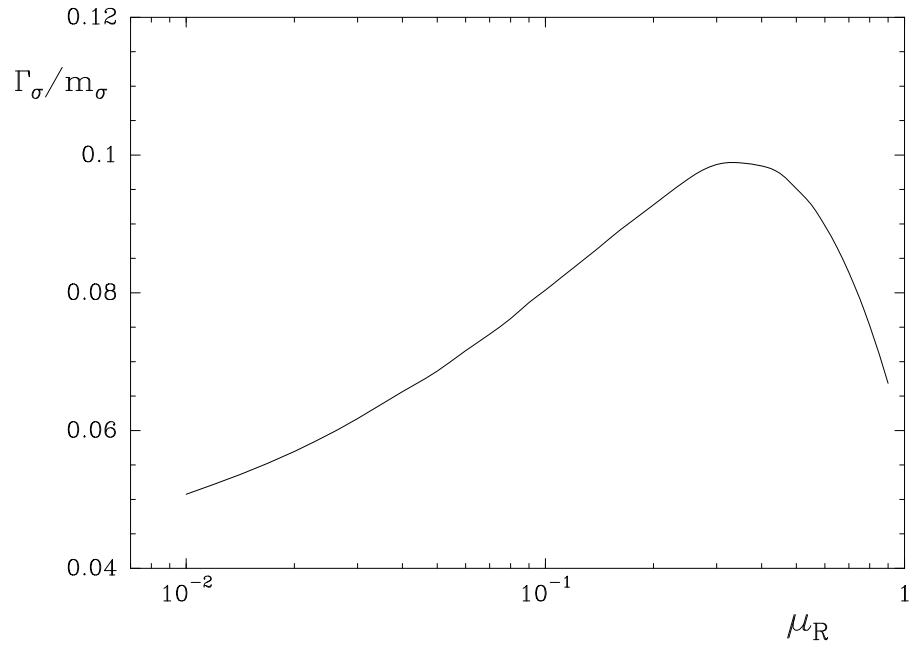


Figure 38: The variation in Γ_σ/m_σ along the curve $\mu_R/m_\pi = 1/2$.

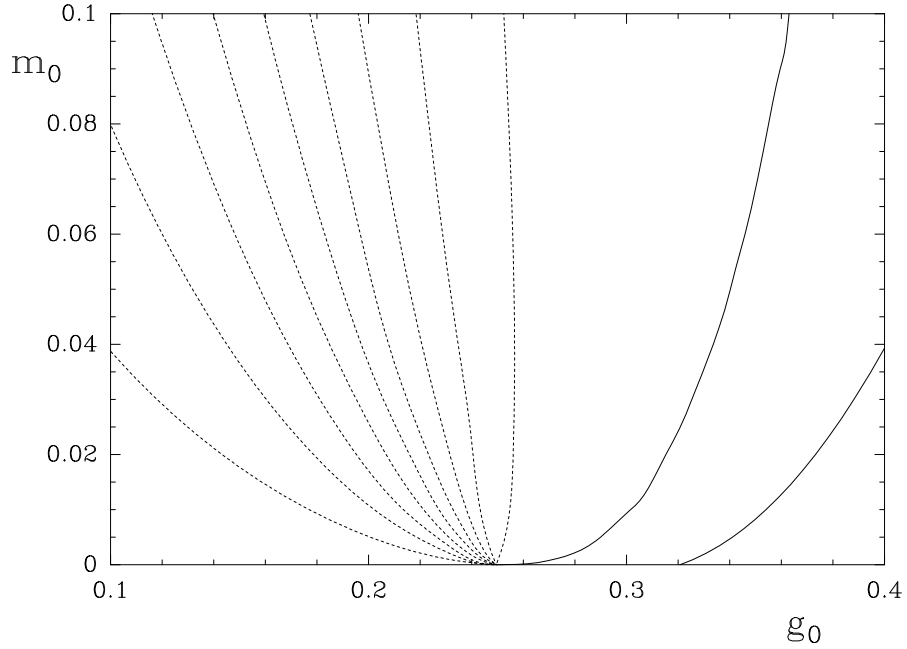


Figure 39: Lines of constant μ_R/m_σ on an ∞^4 lattice. The ratios are 0.51 and 0.50 (bound state and threshold: solid lines); 0.45 to 0.05 in steps of 0.05 (resonance: dashed lines).

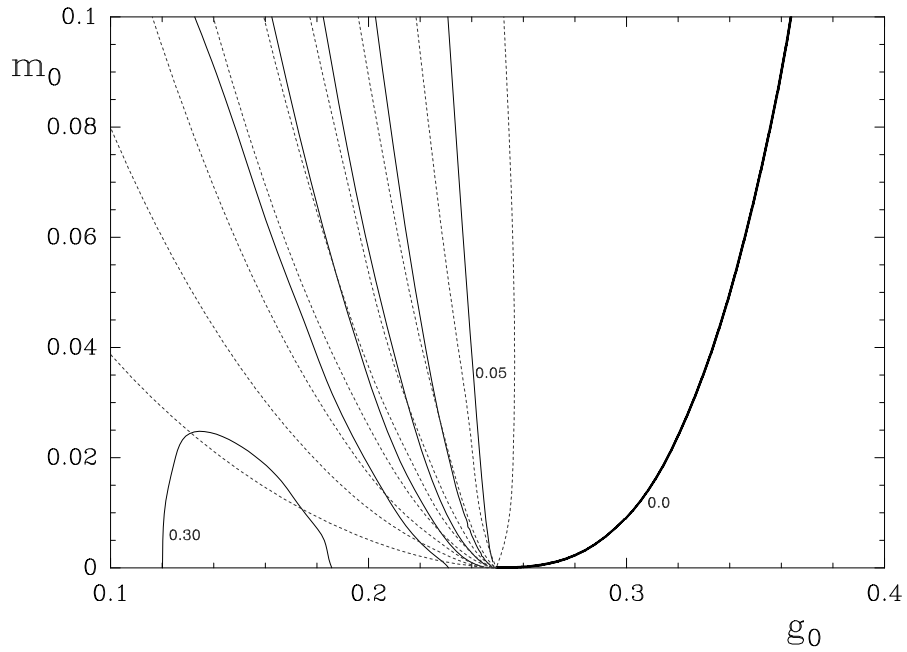


Figure 40: A comparison between the flows of constant Γ_σ/m_σ (solid lines) and constant μ_R/m_σ (dotted lines) in the region where the σ is a resonance. μ_R/m_σ runs from 0.05 to 0.45 in steps of 0.05, Γ_σ/m_σ from 0.0 to 0.3 in steps of 0.05.

and the fermion. As we approach the critical point, μ_R small, this physical coupling decreases, consistent with the hypothesis that the NJL model is trivial.

Note that on the curve $m_\pi = 2\mu_R$, the threshold for pion decay, both Γ_π and f_π vanish. This raises the possibility that this threshold could be a line of constant physics. To check this we have to look at other particles such as the σ . In fig. 38 we plot the variation of the ratio Γ_σ/m_σ along the line $m_\pi = 2\mu_R$. We see that the decay rate of the σ is not constant along this curve, but decreases slowly as we approach the critical point. Fig. 38 is in fact reminiscent of fig. 37, and again consistent with a trivial continuum limit for the NJL model.

In fig. 39 we show the ratio of fermion to σ mass as found from the Schwinger-Dyson equations. Above g_c there is a large region where this ratio is always very close to the value of 0.5 found in [2]. In the symmetric phase the σ is a resonance with a mass similar to that of the π , as would be expected from unbroken chiral symmetry. (Because the σ mass hovers around $2\mu_R$ in the broken phase the mass ratio $E_\sigma^{(0)}/\mu_R$ is essentially constant and a Monte Carlo flow picture shows nothing new.) In fig. 40 we compare the flow patterns for the ratios Γ_σ/m_σ and μ_R/m_σ . As in fig. 36, the corresponding picture for the pion, we see a crossing of the two flows, once again a sign of non-renormalisability.

7 Conclusions

We have made a thorough investigation of a lattice version of the NJL model using both the Monte Carlo method and Schwinger-Dyson equations. The interplay between both methods allowed us to come much further than with either method alone. We extensively used the Schwinger-Dyson equations because of rather large finite size effects.

Since we were interested in the chiral symmetry properties we worked with staggered fermions. A phase transition was seen at about $g_c \approx 0.280(4)$. In the Goldstone π channel we have successfully identified a bound state in the broken phase and a resonance in the symmetric phase. In the σ and ρ channels we have seen resonances. We have found that particles in the π and σ channels become massless at the critical point while particles in the ρ channel scale with the inverse lattice spacing.

Equipped with the results from spectroscopy we worked out renormalisation group flows in the bare parameter plane. We do not find any lines of constant physics: lines of constant μ_R/f_π cross lines of constant m_π/μ_R . The ratio m_σ/μ_R has come out essentially constant in the broken phase and so has no bearing on this question. The absence of renormalisability implies that one should be cautious in applying renormalisation group techniques as is sometimes done in the top-mode standard model.

The NJL model has attracted speculations such as a non-Lorentz invariant vacuum or a massless vector state [4]. These do not appear to be realised at the phase transition that we investigated.

Our lattice model can of course be embedded in a generalized NJL model with more bare parameters [8]. It might then be possible to find regions in this extended parameter space where the model is (weakly) renormalisable. If such a region intersects the part of the parameter space we have studied our physical results (absence of light vector states, occurrence of resonances, etc.) would hold inside this whole region.

We have now reached a comprehensive understanding of the four dimensional NJL-Model concerning the chiral condensate, the fermion mass, meson spectroscopy and renormalisation properties.

Acknowledgements

This work was in part supported by the Deutsche Forschungsgemeinschaft. The numerical calculations were performed on the Fujitsu VP 2400/40 at the RRZN Hannover, the Crays at the ZIB Berlin and the Cray X-MP at the RZ Kiel. We thank all these institutions for their support.

A Schwinger-Dyson Equations for the Composite States

In this appendix we shall derive meson correlation functions using the Schwinger-Dyson equations shown in fig. 14. K is the two particle irreducible kernel, which is in general a function of 4 coordinates, and so on a lattice of volume V has V^4 values. This is reduced by a factor V due to translation invariance. If we consider a fermion-antifermion pair with definite centre of mass momentum p , momentum conservation further reduces this to V^2 values. K can therefore be regarded as a $V \times V$ matrix that links the separation vector of the incoming fermion-antifermion pair (with V possible values) to the relative distance of the outgoing pair. This becomes much more tractable when we replace the full kernel by the bare four fermion interaction. The resulting equations are at the same level of accuracy as the order g_0 Schwinger-Dyson equations which were used for the fermion propagator and the chiral condensate.

Because the bare kernel is very short range, involving only fields separated by distance 0 or 1, we only need the two particle wave function at 9 values of the separation (0 or $\pm\hat{\mu}$). This allows us to write the Schwinger-Dyson equations in a 9×9 matrix form, so we can express the solution of them in terms of the momentum space meson propagators

$$P_{ij}(p) \equiv \frac{1}{V} \langle \mathcal{O}_i(-p) \mathcal{O}_j(p) \rangle, \quad (\text{A.1})$$

where

$$\begin{aligned} \mathcal{O}_0(p) &= \sum_x \bar{\chi}(x) \chi(x) \exp(ip \cdot x), \\ \mathcal{O}_j(p) &= \sum_x \eta_\mu(x) \bar{\chi}(x) \chi(x + \hat{\mu}) \exp(ip \cdot (x + \frac{1}{2}\hat{\mu})), \quad j = 2\mu, \\ \mathcal{O}_j(p) &= \sum_x \eta_\mu(x) \bar{\chi}(x + \hat{\mu}) \chi(x) \exp(ip \cdot (x + \frac{1}{2}\hat{\mu})), \quad j = 2\mu - 1, \end{aligned} \quad (\text{A.2})$$

and $\eta_\mu(x)$ is defined in (2.3). In this basis the four fermion kernel K is given by

$$K = \left(\begin{array}{c} \boxed{-2g_0 \sum_\mu \cos p_\mu} \\ \begin{array}{cc} \boxed{0 \quad g_0} \\ \boxed{g_0 \quad 0} \end{array} \\ \begin{array}{cc} \boxed{0 \quad g_0} \\ \boxed{g_0 \quad 0} \end{array} \\ \begin{array}{cc} \boxed{0 \quad g_0} \\ \boxed{g_0 \quad 0} \end{array} \\ \begin{array}{cc} \boxed{0 \quad g_0} \\ \boxed{g_0 \quad 0} \end{array} \end{array} \right), \quad (\text{A.3})$$

and the Schwinger-Dyson equation reads

$$P = M + MKP. \quad (\text{A.4})$$

As can be seen from the figure M is given by the independent propagation of a fermion and antifermion, i. e., the t -channel disconnected part of P

$$M_{ij}(p) \equiv \frac{1}{V} \langle \mathcal{O}_i(-p) \mathcal{O}_j(p) \rangle_{t\text{-channel disconnected}}. \quad (\text{A.5})$$

Explicitly

$$M = \begin{pmatrix} \boxed{a} & d_1 & -d_1 & d_2 & -d_2 & d_3 & -d_3 & d_4 & -d_4 \\ \boxed{d_1} & c_1 & b_1 & e_{12} & -e_{12} & e_{13} & -e_{13} & e_{14} & -e_{14} \\ \boxed{-d_1} & b_1 & c_1 & -e_{12} & e_{12} & -e_{13} & e_{13} & -e_{14} & e_{14} \\ \boxed{d_2} & e_{12} & -e_{12} & \boxed{c_2} & \boxed{b_2} & e_{23} & -e_{23} & e_{24} & -e_{24} \\ \boxed{-d_2} & -e_{12} & e_{12} & \boxed{b_2} & \boxed{c_2} & -e_{23} & e_{23} & -e_{24} & e_{24} \\ \boxed{d_3} & e_{13} & -e_{13} & e_{23} & -e_{23} & \boxed{c_3} & \boxed{b_3} & e_{34} & -e_{34} \\ \boxed{-d_3} & -e_{13} & e_{13} & -e_{23} & e_{23} & \boxed{b_3} & \boxed{c_3} & -e_{34} & e_{34} \\ \boxed{d_4} & e_{14} & -e_{14} & e_{24} & -e_{24} & e_{34} & -e_{34} & \boxed{c_4} & \boxed{b_4} \\ \boxed{-d_4} & -e_{14} & e_{14} & -e_{24} & e_{24} & -e_{34} & e_{34} & \boxed{b_4} & \boxed{c_4} \end{pmatrix}. \quad (\text{A.6})$$

The ‘‘bubbles’’ (see fig. 41) in M are

$$\begin{aligned} a(p) &= \frac{1}{V} \sum_k \frac{N^2 - \sum_\mu F_\mu^2 s_\mu^+ s_\mu^-}{U^+ U^-}, \\ b_\mu(p) &= -\frac{1}{V} \sum_k \frac{F_\mu^2 s_\mu^+ s_\mu^- - \sum_{\nu \neq \mu} F_\nu^2 s_\nu^+ s_\nu^- - N^2}{U^+ U^-}, \\ c_\mu(p) &= \frac{1}{V} \sum_k \frac{(F_\mu^2 s_\mu^+ s_\mu^- - \sum_{\nu \neq \mu} F_\nu^2 s_\nu^+ s_\nu^- - N^2) (1 - 2(s_\mu^0)^2)}{U^+ U^-}, \\ d_\mu(p) &= \frac{1}{V} \sum_k \frac{N F_\mu (s_\mu^+ + s_\mu^-) s_\mu^0}{U^+ U^-}, \\ e_{\mu\nu}(p) &= -\frac{1}{V} \sum_k \frac{F_\mu F_\nu (s_\mu^+ s_\nu^- + s_\mu^- s_\nu^+) (c_\mu^0 c_\nu^0 + s_\mu^0 s_\nu^0)}{U^+ U^-}, \end{aligned} \quad (\text{A.7})$$

where

$$\begin{aligned} s_\mu^\pm &\equiv \sin(k_\mu \pm \frac{1}{2} p_\mu), \\ s_\mu^0 &\equiv \sin k_\mu, \\ c_\mu^0 &\equiv \cos k_\mu, \\ U^\pm &\equiv N^2 - \sum_\mu F_\mu^2 (s_\mu^\pm)^2, \end{aligned} \quad (\text{A.8})$$

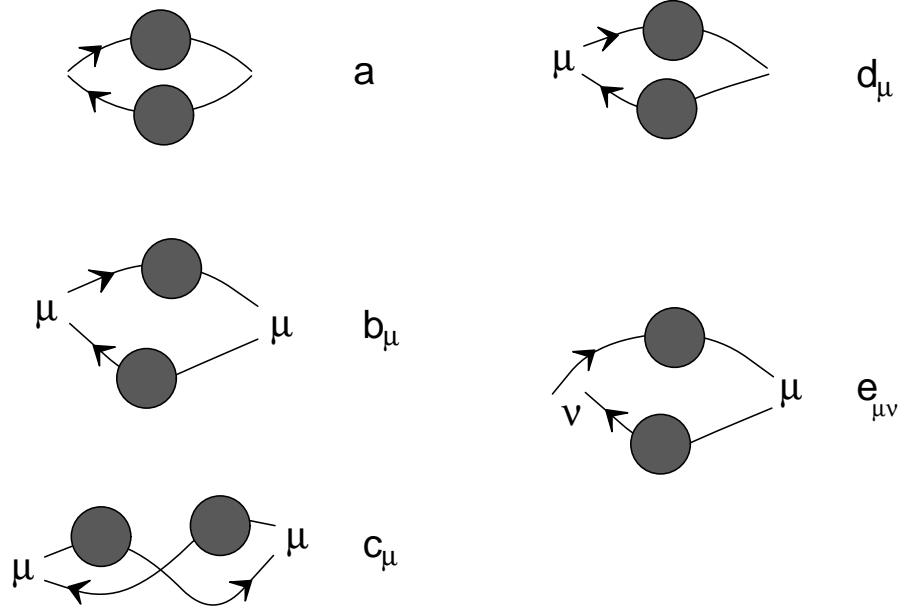


Figure 41: Graphical representation of the “bubbles” in eqs. (A.6) and (A.7).

and N , F_μ are given in (2.14). Equation (A.4) is solved by

$$P = (\mathbf{1} - MK)^{-1}M. \quad (\text{A.9})$$

This is the full solution including the annihilation term. The matrix inversion is done numerically.

Because we are working with staggered fermions we get mesons at rest if the spatial components of p are all either 0 or π . Other values of \vec{p} give moving mesons and can be used to check the restoration of Lorentz invariance.

In most of our Monte Carlo calculations we have measured only the fermion line connected part of the meson propagator as is customary. This means that t-channel exchange of auxiliary fields is kept, but s-channel (i. e., annihilation) auxiliary fields are dropped (see eq. (4.6)). When we make this same approximation in the Schwinger-Dyson equations only the first term in the kernel is kept. We no longer have to consider bond operators, so the 9×9 matrix becomes a 1×1 matrix. The meson propagator simplifies to

$$\begin{aligned} P(p) &\equiv \sum_x \langle (\bar{\chi}\chi)(x)(\bar{\chi}\chi)(0) \rangle e^{-ip \cdot x} \\ &= \frac{a(p)}{1 + a(p)2g_0 \sum_\mu \cos p_\mu}. \end{aligned} \quad (\text{A.10})$$

The propagator $P(p)$ includes the first four multiplets shown in table 7 because the s -factors in the table are all of the form $\exp(ip \cdot x)$, i. e., all represent a simple shift in momentum in eq. (A.10). We are most interested in the propagators $C_i^{(0)}(t)$ for stationary mesons, i. e., mesons for which $\vec{p} = 0 \bmod \pi$. Let the Fourier transform of $C_i^{(0)}(t)$ be $\tilde{C}_i^{(0)}(\omega)$ (see eq. (4.13) for normalisation). The channel $i = 1$ (the π'/σ channel) corresponds to

$$\tilde{C}_1^{(0)}(\omega) = P(0, 0, 0, \pi + \omega), \quad (\text{A.11})$$

$i = 2$ (the π channel) corresponds to

$$\tilde{C}_2^{(0)}(\omega) = P(\pi, \pi, \pi, \pi + \omega), \quad (\text{A.12})$$

and the ρ'/a and ρ/b channels ($i = 3, 4$) to

$$\tilde{C}_3^{(0)}(\omega) = P(\pi, 0, 0, \pi + \omega) = P(0, \pi, 0, \pi + \omega) = P(0, 0, \pi, \pi + \omega) \quad (\text{A.13})$$

and

$$\tilde{C}_4^{(0)}(\omega) = P(0, \pi, \pi, \pi + \omega) = P(\pi, 0, \pi, \pi + \omega) = P(\pi, \pi, 0, \pi + \omega) \quad (\text{A.14})$$

respectively. Representing the \tilde{C} 's as particular values of $P(p)$ shows that the fact that the different i and k channels don't mix is simply a consequence of the conservation of 3-momentum. Inserting the above momentum values in (A.10) gives the results stated in eq. (4.14).

B The Infinite Volume Limit of the Meson Propagators

In this appendix we study the infinite volume limit of the meson propagators (4.14). We have already taken the $L_t \rightarrow \infty$ limit in (4.20). We now let $L_s \rightarrow \infty$. In the infinite volume limit the different boundary conditions in the space and time directions no longer matter and so $F_s = F_t \equiv F$.

The fermion loop integrals in (4.18) are all of the form

$$\int_0^{2\pi} \frac{dk_1}{2\pi} \frac{dk_2}{2\pi} \frac{dk_3}{2\pi} h(\sin^2 k_1 + \sin^2 k_2 + \sin^2 k_3). \quad (\text{B.1})$$

In the continuum we would naturally simplify such a ‘spherically symmetric’ integral by changing variables to $k_1^2 + k_2^2 + k_3^2$. In the same way we use the variable

$$r = -3 + 2(\sin^2 k_1 + \sin^2 k_2 + \sin^2 k_3) \quad (\text{B.2})$$

to simplify the lattice integrals. (The shift and normalisation make some of the following expressions simpler than they would otherwise be.) The integral (B.1) then becomes

$$\int_{-3}^3 dr h\left(\frac{3}{2} + \frac{1}{2}r\right) \phi(r). \quad (\text{B.3})$$

The ‘phase space’ function ϕ is

$$\begin{aligned} \phi(r) &= \int_0^{2\pi} \frac{d^3k}{(2\pi)^3} \delta(r + 3 - 2(\sin^2 k_1 + \sin^2 k_2 + \sin^2 k_3)) \\ &= \int_{-\infty}^{+\infty} \frac{d\nu}{2\pi} e^{i\nu r} J_0^3(\nu). \end{aligned} \quad (\text{B.4})$$

ϕ is 0 outside the range $(-3, 3)$ and has branch points at $r = \pm 1$. These branch points are relevant to the analytic structure of the spectral density.

Expressing the A ’s and B ’s in eqs. (4.15) and (4.16) in terms of r and using eq. (2.15) to eliminate N gives

$$\begin{aligned} A^2 &= F^2 \left(\sinh^2 \mu_R + (r + 3)/2 \right), \\ B_1^2 &= F^2 \left(\sinh^2 \mu_R - (r + 3)/2 \right), \\ B_2^2 &= F^2 \left(\sinh^2 \mu_R + (r + 3)/2 \right), \\ B_3^2 &= F^2 \left(\sinh^2 \mu_R - (r + 3)/6 \right), \\ B_4^2 &= F^2 \left(\sinh^2 \mu_R + (r + 3)/6 \right). \end{aligned} \quad (\text{B.5})$$

We have now reduced our original four-dimensional integrals to one dimensional integrals from which we can find the analytic structure of $a_i(\omega)$ and therefore also of $\tilde{C}_i(\omega)$. In an infinite volume $a_i(\omega)$ is given by an integral of the form

$$a_i(\omega) = \frac{1}{F^2} \int_{-3}^3 dr \phi(r) \left(\frac{f_+(r)}{2 \sinh^2 \mu_R + r + 4 - \cos \omega} - \frac{f_-(r)}{2 \sinh^2 \mu_R + r + 4 + \cos \omega} \right). \quad (\text{B.6})$$

$f_+(r)$ and $f_-(r)$ are analytic (and real) in $(-3, 3)$. The ensuing singularity structure is sketched in fig. 15 and discussed in the main text.

References

- [1] E. Fermi, *Z. Phys.* **88** (1934) 161.
- [2] Y. Nambu and G. Jona-Lasinio, *Phys. Rev.* **122** (1961) 345.
- [3] J. Goldstone, *Nuovo Cim.* **19** (1961) 154.
- [4] J.D. Bjorken, *Ann. Phys.* **24** (1963) 174;
I. Bialynicki-Birula, *Phys. Rev.* **130** (1963) 465;
T. Eguchi and H. Sugawara, *Phys. Rev.* **D10** (1974) 4257;
D. Amati, R. Barbieri, A.C. Davis and G. Veneziano, *Phys. Lett.* **B102** (1981) 408;
T. Banks and A. Zaks, *Nucl. Phys.* **B184** (1981) 303.
- [5] E. Farhi and L. Susskind, *Phys. Rep.* **3** (1981) 277;
B. Holdom, *Phys. Lett.* **B150** (1985) 301; *ibid.* **B198** (1987) 535;
K. Yamawaki, M. Bando and K. Matumoto, *Phys. Rev. Lett.* **56** (1986) 1335;
T. Akiba and T. Yanagida, *Phys. Lett.* **B169** (1986) 432;
T. Appelquist and L.C.R. Wijewardhana, *Phys. Rev.* **D36** (1987) 563.
- [6] Y. Nambu, in *1988 International Workshop on New Trends in Strong Coupling Gauge Theories*, p. 3, eds. M. Bando, T. Muta and K. Yamawaki (World Scientific, Singapore, 1989); in *Proceedings of 1989 Workshop on Dynamical Symmetry Breaking*, p. 1, eds. T. Muta and K. Yamawaki (Nagoya University, Nagoya, 1990);
V.A. Miranski, M. Tanabashi and K. Yamawaki, *Phys. Lett.* **B221** (1989) 177; *Mod. Phys. Lett.* **A4** (1989) 1043;
W. Bardeen, C. Hill and M. Lindner, *Phys. Rev.* **D41** (1990) 1647;
W.J. Marciano, *Phys. Rev. Lett.* **62** (1989) 2793;
W. Suzuki, *Phys. Rev.* **D41** (1990) 3457; *Mod. Phys. Lett.* **A5** (1990) 1205.
- [7] K. Wilson, *Phys. Rev.* **D7** (1973) 2911.
- [8] A. Hasenfratz, P. Hasenfratz, K. Jansen, J. Kuti and Y. Shen, *Nucl. Phys.* **B365** (1991) 79;
J. Zinn-Justin, *Nucl. Phys.* **B367** (1991) 105.
- [9] A. Hasenfratz and P. Hasenfratz, *Phys. Lett.* **B297** (1992) 166.
- [10] C.N. Leung, S.T. Love and W.A. Bardeen, *Nucl. Phys.* **B273** (1986) 649;
K.-I. Kondo, M. Tanabashi and K. Yamawaki, *Prog. Theor. Phys.* **89** (1993) 1249;
P.E.L. Rakow, in *1990 International Workshop on Strong Coupling Gauge Theories and Beyond*, p. 249, eds. T. Muta and K. Yamawaki (World Scientific, Singapore, 1991); *Nucl. Phys.* **B356** (1991) 27.

- [11] M. Göckeler, R. Horsley, P. Rakow, G. Schierholz and R. Sommer, Nucl. Phys. **B371** (1992) 713.
- [12] F.J. Dyson, Phys. Rev. **75** (1949) 1736;
J. Schwinger, Proc. Natl. Acad. Sci. U. S. **31** (1951) 455.
- [13] P. Roman, *Introduction to Quantum Field Theory*, John Wiley and Sons (1969).
- [14] H. Stüben, *Ph. D. Thesis*, Freie Universität Berlin (1993).
- [15] I.-H. Lee and R.E. Shrock, Phys. Rev. Lett. **59** (1987) 14.
- [16] S.P. Booth, R.D. Kenway and B.J. Pendleton, Phys. Lett. **B228** (1989) 115.
- [17] K. Bitar, A.D. Kennedy, R. Horsley, S. Meyer and P. Rossi, Nucl. Phys. **B313** (1989) 348.
- [18] P. Rossi and J.H. Sloan, *preprint* UCSD-PTH-89-10 (1989).
- [19] J.S. Kouvel and M.E. Fisher, Phys. Rev. **136** (1964) A 1626.
- [20] J. Gasser and H. Leutwyler, Phys. Lett. **B188** (1987) 477.
- [21] M.F.L. Golterman, Nucl. Phys. **B273** (1986) 663.
- [22] R. Altmeyer, K.D. Born, M. Göckeler, R. Horsley, E. Laermann and G. Schierholz, Nucl. Phys. **B389** (1993) 445.
- [23] G. Kilcup, Nucl. Phys. **B** (Proc. Suppl.) **9** (1989) 201.
- [24] M. Lüscher, Nucl. Phys. **B364** (1991) 237.
- [25] G.W. Kilcup and S.R. Sharpe, Nucl. Phys. **B283** (1987) 493.
- [26] A. Patel, Phys. Lett. **B141** (1984) 244.
- [27] L. van Hove, Phys. Rev. **89** (1953) 1189;
J.M. Ziman, *Principles of the Theory of Solids*, Cambridge University Press (1964).
- [28] R.J. Eden, P.V. Landshoff, D.I. Olive and J.C. Polkinghorne, *The Analytic S-Matrix*, Cambridge University Press (1966).
- [29] G.P. Lepage, *Cornell preprint* CLNS 89/970 (1989).
- [30] L.M. Brown, ed., *Renormalization*, Springer Verlag (1993).